Magnetotelluric imaging of lower crustal melt and lithospheric hydration in the Rocky Mountain Front transition zone, Colorado, USA

D. W. Feucht[1,2], A. F. Sheehan[1,2], and P. A. Bedrosian[3]

[1]Department of Geological Sciences, University of Colorado Boulder, Boulder, Colorado, USA, [2]Cooperative Institute for Research in Environmental Sciences, University of Colorado Boulder, Boulder, Colorado, USA, [3]Crustal Geophysics and Geochemistry Science Center, U.S. Geological Survey, Denver, Colorado, USA.

Corresponding author: Daniel Feucht (daniel.feucht@colorado.edu)

Key Points:

- We image 2D anisotropic electric resistivity structure beneath the Rocky Mountains and Great Plains to depths of 150 km
- High electrical conductivity in the lower crust beneath the Rocky Mountains is attributed to partial melt and crustal fluids
- Eastward deepening mantle conductivity beneath the Great Plains is interpreted as a hydration front

Abstract

We present an electrical resistivity model of the crust and upper mantle from two-dimensional (2D) anisotropic inversion of magnetotelluric data collected along a 450 km transect of the Rio Grande Rift, southern Rocky Mountains, and High Plains in Colorado, USA. Our model provides a window into the modern-day lithosphere beneath the Rocky Mountain Front to depths in excess of 150 km. Two key features of the 2D resistivity model are (1) a broad zone (~200 km wide) of enhanced electrical conductivity (<20 Ωm) in the mid- to lower-crust that is centered beneath the highest elevations of the southern Rocky Mountains and (2) hydrated lithospheric mantle beneath the Great Plains with water content in excess of 100 ppm. We interpret the high conductivity region of the lower crust as a zone of partially-molten basalt and associated deep-crustal fluids that is the result of recent (less than 10 Ma) tectonic activity in the region. The recent supply of volatiles and/or heat to the base of the crust in the late Cenozoic implies that modern-day tectonic activity in the western United States extends to at least the western margin of the Great Plains. The transition from conductive to resistive upper mantle is caused by a gradient in lithospheric modification, likely including hydration of nominally anhydrous minerals, with maximum hydration occurring beneath the Rocky Mountain Front. This lithospheric "hydration front" has implications for the tectonic evolution of the continental interior and the mechanisms by which water infiltrates the lithosphere.

1. Introduction

1.1 Geologic and Tectonic Background

The Rocky Mountain Front (RMF) is a north-south trending physiographic boundary in the west-central United States that separates the Great Plains to the east from the Rocky Mountains and Basin and Range to the west [*Fenneman* 1946]. The Great Plains are characterized by a low-relief landscape, broad flat sedimentary packages, and anomalously high topography (>1600 m) over a broad region east of the Rocky Mountain Front [*Eaton* 1987]. This topography slopes gently down to the east for nearly 900 km, finally reaching elevations <300 m at the Missouri River on the eastern border of Kansas. The absence of major faulting, structural dismemberment, and volcanism suggest that the high western plains immediately adjacent to the RMF have been largely undeformed since the Proterozoic assembly of the North American continent. Exceptions to this include (1) tilting, subsidence, and rebound in response to Farallon slab subduction, sedimentation, and subsequent slab removal [*Mitrovica et al*., 1989; *Dickinson et al*., 1988] and (2) anorogenic uplift related to lithospheric modification and de-densification caused by hydration of the lithosphere during Farallon slab subduction [*Humphreys et al.,* 2003, *Jones et al*., 2015].

In contrast, the mountains to the west of the RMF are characterized by high relief and topography, with the southern Rocky Mountains in Colorado representing the most significant collection of high peaks on the North American plate [*Eaton* 2008]. The modern landscape of the southern Rocky Mountains is the result of a protracted tectonic history extending at least as far back in time as the formation of the Ancestral Rocky Mountains in the Pennsylvanian [*Mallory* 1958]. Since just the late Cretaceous, the region has been subjected to basement-cored thrust faulting associated with the Laramide orogeny [*DeCelles* 2004], high-volume silicic volcanism in the Paleogene [*Lipman* 1992], widespread landscape beveling during the Eocene [*Epis and Chapin*, 1975], and at least two distinct episodes of continental rifting along the Rio Grande Rift

from the Oligocene to the modern day [*Chapin and Cather*, 1994; *Landman and Flowers*, 2013]. Quaternary fault scarps [*Tweto* 1979], geodetic observations [*Berglund et al*., 2012], seismicity [*Nakai et al*., 2017], and recent volcanism [*Leat et al*., 1989] suggest that the southern Rocky Mountains are tectonically active in the present day.

1.2 Previous Geophysical Results

Geophysical studies on both regional and continental scales suggest that the physiographic contrast observed across the Rocky Mountain Front is at least coincident with, if not indicative of, a more profound lithospheric discontinuity at depth [*Pakiser and Zietz*, 1965]. Investigations into seismic velocity of the crust and upper mantle and seismic attenuation suggest the Rocky Mountain Front delineates the transition between younger, actively deforming lithosphere of western North America and older, more stable Proterozoic lithosphere to the east [*Boyd and Sheehan*, 2005; *Phillips et al*., 2014; *Schmandt and Lin*, 2014; *Schmandt et al*., 2015].

Teleseismic shear-wave travel time residuals recorded by the Rocky Mountain Front PASSCAL experiment show a distinct increase in residual delay times from east to west across the Rocky Mountain Front [*Lee and Grand*, 1996]. Subsequent tomographic inversions of those delay times reveal a low-velocity mantle (shear-wave velocity anomalies as low as -4.5% relative to PREM 1981 at depths of 50-100 km) beneath the southern Rocky Mountains in central Colorado [*Lee and Grand*, 1996]. *Li et al*. [2002] inverted Rayleigh-wave phase velocities from the same experiment to show that there is also a crustal low-velocity zone (shear-wave velocity anomaly as low as -4% relative to a modified version of AK135) beneath the highest topography in Colorado. Recent analysis of seismic data from the EarthScope USArray and co-deployed regional seismic networks (e.g. CREST [*Hansen et al*., 2013]) have produced a multitude of seismic-velocity models of the western United States and Rocky Mountain Front [e.g. *Schmandt and Humphreys*, 2010; *Shen et al*., 2013; *Hansen et al*. 2013, *Porritt et al*., 2014; *Schmandt and Lin*, 2014]. A broad low-velocity zone in the upper mantle beneath Colorado west of the RMF is a common feature of each of these models. Possible explanations for the anomaly include both thermal and compositional variations in the upper mantle, including both thinned and/or chemically modified lithosphere. Low velocity anomalies in the lower crust are typically attributed to compositional variations, specifically an abundance of low-density felsic material in the crust west of the Rocky Mountain Front [*Decker et al*., 1988; *Li et al*., 2002; *Schmandt et al*., 2015].

The magnetotelluric (MT) method is particularly well suited for differentiating thermal and compositional origins of geophysical anomalies within the lithosphere [e.g., *Yang et al*., 2011; *Wannamaker et al.*, 2008; *Li et al*., 2003] , where resolution is comparable to seismic tomography [e.g. *Meqbel et al*., 2014]. In this paper we present results from a magnetotelluric survey in central Colorado that straddles the Rocky Mountain Front. We employ a 2-D anisotropic inverse modeling approach to determine electrical resistivity structure beneath our profile. We image (1) a zone of high conductivity in the lower crust beneath the southern Rocky Mountains and (2) distinct compositional modification of the lithospheric mantle beneath the western edge of the Great Plains. We examine the possible compositional and thermal origins of these anomalies before commenting on the tectonic implications of our preferred interpretation.

2. Methods and Data

2.1 Magnetotellurics

Magnetotelluric data is collected by measuring spatial and temporal variations in the naturally occurring electric (E) and magnetic (H) fields at the surface of the earth. The magnetotelluric impedance tensor (Z) is a second-rank complex tensor that in the frequency domain relates horizontal magnetic fields to horizontal electric fields by

$$\begin{bmatrix} E_X \\ E_Y \end{bmatrix} = \begin{bmatrix} Z_{XX} & Z_{XY} \\ Z_{YX} & Z_{YY} \end{bmatrix} \cdot \begin{bmatrix} H_X \\ H_Y \end{bmatrix} \quad (1)$$

The four components of the complex, frequency-dependent impedance tensor can be represented as scaled amplitude (apparent resistivity, ρ_a, units of Ωm) and phase. The magnetic-field transfer function (T), or tipper, is a complex unitless vector quantity that relates the horizontal magnetic field to the vertical magnetic field by

$$H_Z = \begin{bmatrix} T_X & T_Y \end{bmatrix} \cdot \begin{bmatrix} H_X \\ H_Y \end{bmatrix} \quad (2)$$

These transfer functions vary both spatially according to the electrical resistivity structure of the subsurface and with frequency as a function of changes in subsurface resistivity with depth. A magnetotelluric sounding consists of estimates of impedance and tipper as a function of period, obtained via spectral analysis of electromagnetic-field time series. The depth of investigation of each sounding depends on both the period (the inverse of frequency) and the local electrical resistivity structure, with longer periods and a more resistive subsurface allowing for a greater depth of investigation.

The magnetotelluric method is in particular sensitive to electrical resistivity, or its reciprocal conductivity, which is dependent upon mineralogy, fluid content, partial melting, and chemical alteration of the subsurface. Sources of high conductivity in sedimentary basins and within the brittle upper crust include clay minerals, fault gouge, and groundwater. The primary controls on electrical conductivity in the lower crust are the abundance and interconnectedness of aqueous fluid, small volumes of partial melt, and grain boundary mineralization. Electrical conductivity in the upper mantle is primarily controlled by the concentration of water in nominally-anhydrous minerals [*Poe et al*., 2010; *Dai and Karato*, 2009], the presence of partial melt, and to a lesser extent the bulk temperature of the rock [*Constable et al*., 1992].

2.2 Data

Twenty-three magnetotelluric soundings were collected in central Colorado along a 450 km profile located at 39.2ºN latitude (Figure 1). Details on the data acquisition parameters can be found in the Supplementary Material. Time-series processing and transfer-function estimation was performed using the approach of *Egbert* [1997] for multi-station arrays with remote referencing [*Gamble et al*., 1979]. Some stations required additional pre-processing prior to transfer function estimation due to operator error, data logger malfunction, and/or station disturbance during recording. Pre-processing steps included trimming of data contaminated by cultural noise, scaling, and correction of layout errors (e.g. electric and magnetic channel flips). Figure 2 shows representative transfer function curves for two stations: stn016 located in the mountains and stn024 in the plains.

The magnetotelluric phase tensor [*Caldwell et al*., 2004], a mathematical transformation of the impedance tensor, is used to examine the dimensionality of MT data. Interpretation of the phase tensor is performed by examining maps of normalized phase tensor ellipses, the major and

minor axes of which are proportional to the rotationally-invariant maximum and minimum principle values of the represented phase tensor. Circular phase tensors reflect a one-dimensional impedance (layer-cake subsurface resistivity structure) while non-circular ellipses indicate higher-order electrical resistivity structure (e.g. lateral variations in resistivity). In the two-dimensional (2D) case, the major axis of the ellipse will align either perpendicular or parallel to the predominant geo-electric strike for data collected on the conductive or resistive side, respectively, of a geo-electrical contact.

Figure 1 shows normalized phase tensor ellipses for all 23 MT stations at a period of 1000 s. Note the major-axis orientation of the phase tensor ellipses changes from generally north-south to east-west moving west to east across the Rocky Mountain Front, indicating a major geo-electric contact coincident with the Rocky Mountains-Great Plains physiographic boundary. The scalar value β, another rotationally-invariant phase tensor parameter, is an indicator of three-dimensional (3D) geo-electric structure. Typically, $|\beta| > 3^{\circ}$ is considered an indication of 3D structure [*Booker* 2014]. The majority of the ellipses in Figure 1 exhibit low values of β (see fill color) with either major or minor axes trending sub-parallel to the profile, indicating that two-dimensional inversion of the measured data is justified. We note high β values are observed for several stations in the mountains (106ºW-105ºW) at period of 1000 s. Given the high resistivity of the plutonic and metamorphic rocks of the Rocky Mountain Front Range that underlie these particular stations, the phase tensors at the displayed period may have sensitivity to mid- to lower crustal structure, indicating that the geoelectric structure is complex at depth. Quasi-3D electrical resistivity structure is also observed in the distribution of induction vector orientations (see Supplementary Material, Figure S1). The ability of the 2D anisotropic inversion to fit these pseudo 3D data is shown in Figure 2a for stn016. Full pseudo-sections of observed data and anisotropic model fits are provided in the Supplementary Material.

2.3 2-D Inversion

We invert for two-dimensional isotropic and anisotropic electrical resistivity structure along our profile using the finite-element inversion algorithm MARE2DEM [*Key* 2016]. The MARE2DEM algorithm utilizes an Occam's inversion approach [*Constable et al*., 1987], which seeks to iteratively determine the smoothest possible electrical resistivity structure that minimizes the functional

$$U = \| \boldsymbol{\partial}\mathbf{m} \|^2 + \mu^{-1}\left[\| \mathbf{W}\left(\mathbf{d} - F(\mathbf{m})\right) \|^2 - \chi^2 \right] \quad (3)$$

where $\mathbf{d}$ is the magnetotelluric data, $F(\mathbf{m})$ is the forward MT response [*Key and Ovall*, 2011], $\mathbf{W}$ is a diagonal matrix of inverse data standard errors, μ is a regularization factor, χ^2 is a user-defined misfit tolerance, and $\boldsymbol{\delta}\mathbf{m}$ is a model roughness term. The inversion progresses by first automatically sweeping through values of μ to find the best fitting model and iterating until the χ^2 target misfit is achieved. The second phase of the inversion involves searching for the smoothest model that also achieves the desired misfit. Model updates are performed at each iteration via linearizing the functional about a starting model. The inclusion of the χ^2 tolerance in the functional allows the inversion to avoid extreme local minima based on select noisy or non-physical data. Data fit is assessed using a root mean square misfit that is normalized by data errors and the number of variables

$$\mathrm{RMS} = \sqrt{\frac{1}{n}\sum_{i=1}^{n}\left[\frac{d_i - F_i(\mathbf{m})}{s_i}\right]^2} \quad (4)$$

where d_i and $F_i(m)$ are an individual datum and corresponding forward response, s_i is data uncertainty and n is the total number of data points.

Anisotropy for the purposes of this study refers to strictly horizontal (or transverse) anisotropy, wherein the electrical resistivity of each grid cell is allowed to vary in two directions: parallel (ρ_{yy}) and perpendicular (ρ_{xx}) to the profile trace. It is expected that transverse anisotropic structure oriented at an oblique angle to the profile trace will partition into ρ_{xx} and ρ_{yy} components. Anisotropy is incorporated into the inversion through the model roughness term, which contains a measure of the difference between the ρ_{xx} and ρ_{yy} resistivity models, regularized by an anisotropy penalty factor, α. The value of α varies from 0 (completely anisotropic) to 1 (isotropic) and is defined by the user prior to inversion. For the anisotropic inverse models shown in this study we set $\alpha = 0.1$ to allow the structure to vary in both anisotropic directions.

2.4 Data Preparation

Inputs into the inversion include apparent resistivity and phase of the principal impedances (Z_{XY} and Z_{YX}) and the complex 2D component of the tipper (T_Y). The apparent resistivity of the transverse electric (TE) mode, $\rho_{a,xy}$, was omitted from the inversion input due to its sensitivity to off-profile (i.e. 3D) electrical resistivity structure [*Wannamaker et al*., 1984]. The remaining data were decimated to five periods per decade, yielding a total of 30 inverted periods distributed logarithmically over six decades (0.01 - 10,923 s). A subset of the decimated data (~13%) was manually culled via visual inspection of transfer function curves to eliminate obvious outliers. In total, 2496 data points distributed across all 23 stations were inverted for 2D isotropic and anisotropic resistivity structure. Prior to inversion, data errors for apparent resistivity and phase were increased to a minimum threshold, or error floor, of 10% $|Z_{ij}|$, corresponding to an error in phase of 2.8º, to reduce the likelihood of over-fitting data points with exceptionally small statistically-determined errors. An error floor of 0.03 was applied to all tipper components. Data inputs for the isotropic and anisotropic inversions were identical.

2.5 Mesh Preparation

Resistivity models for each inversion were parameterized as unstructured meshes using the graphical user interface Mamba2D (http://mare2dem.ucsd.edu/). Mamba2D is a MATLAB based program that uses Delaunay triangulation to automatically populate regions within the mesh with triangular grid cells of uniform size, where size is defined by the nominal side length of each triangular grid cell. An "area of interest" extending from the surface to 150 km depth (approximately one-third of the survey aperture) and 25 km laterally beyond the first and last stations along the profile was divided into three layers. The three horizontal layers are parameterized as follows: 2 km triangles for 0-10 km depth, 5 km triangles for 10-60 km depth, and 10 km triangles for 60-150 km depth. Outside the region of interest, triangles are allowed to grow exponentially in size towards the edges of the model domain that extends 1000 km in all directions. The atmosphere is parameterized as a 1000 km thick layer with a fixed resistivity value of 1×10^9 Ωm. Topography is not incorporated into the model. The resistivity of the isotropic half-space starting model, 30 Ωm, was selected by determining which among a series of isotropic half-space models with varying resistivity values exhibited the smallest initial misfit to

the data. Model grid parameterization and the starting model for each of the isotropic and anisotropic inversions were identical.

3. Results

3.1 Inversion Results

Figures 3 shows the isotropic resistivity model obtained by inverting the magnetotelluric data along our profile. This model achieved an RMS of 1.3 given the applied errors, representing an 88% reduction in data residual relative to the starting model (initial RMS of 11.3). The alternating pattern of vertical conductive and resistive anomalies visible in the mid-crust to upper mantle (25-100 km depth) is reminiscent of the modeling results of *Heise and Pous* [2001] on the isotropic inversion of anisotropic data. They observed that 2D isotropic inversions of azimuthally anisotropic magnetotelluric data produce characteristic artifacts in modeled resistivity structure, including alternating regions of high and low resistivity. Motivated by these previous findings and the clear pattern seen in Figure 3, we performed a similar modeling study using MARE2DEM. The results of that study, which can be found in the Supplementary Material, support the hypothesis that some of the structure observed in the isotropic model in Figure 3 is an artifact introduced by insufficient modeling of anisotropic data (Figure S2). For the purposes of model analysis and interpretation going forward we will focus on the anisotropic inversion results.

Figure 4 shows our preferred 2D horizontally-anisotropic resistivity model. The models in Figures 4a and 4b show the electrical resistivity structure perpendicular (ρ_{xx}) and parallel (ρ_{yy}) to profile, respectively. The ρ_{xx} model reflects the resistance to north-south current flow in the direction parallel to inferred geoelectric strike. After seven iterations, our preferred model achieved an RMS of 1.2 given the applied errors, representing an 89% variance reduction relative to the starting model (initial RMS of 11.3). The forward response of the final model and data fits for two representative stations are shown in Figure 2. Pseudo-sections of the observed data and model response for all stations can be found in the Supplementary Material (Figure S5).

3.2 Upper Crust

The shallow crust (0-10 km depth) along the profile is resistive with the exception of three thin conductors at or near the surface. These conductors range in resistivity from 5-30 Ωm and correlate with the known sedimentary basins labeled in Figure 1. These basins and the corresponding labels in Figure 4 are, from east to west, the westward-thickening Denver Basin (C3), the South Park Basin (C2), and the Piceance Basin (C1). The upper crust (0-25 km) outside these conductors is generally resistive (>100 Ωm), reaching a maximum value of 1000 Ωm beneath the Rocky Mountain Front Range (105ºW-106.5ºW).

3.3 Lower Crust

The crust beneath the Rocky Mountains is electrically conductive (low resistivity) from mid-crustal depths of 25-35 km to the base of the crust at 45-50 km depth [Moho estimates provided by *Sheehan et al*., 1995; *Gilbert* 2012, *Shen et al*., 2013]. Dense station coverage on the west and east ends of this lower crustal conductor (LCC) constrains its width to ~200 km, from western Colorado to just east of the South Park Basin. Model sensitivity testing (Supplementary Material, Figure S4) confirms that the data supports a laterally continuous LCC despite the ~100 km gap in station coverage (Figure 1). Magnetotellurics is primarily sensitive to the conductance (conductivity-thickness product) of conductors, and thus there is a trade off between the

resolvable thickness and absolute conductivity of the LCC (see Supplementary Material, Figure S3). Figure 5 shows the vertically integrated conductance along the profile of both the ρ_{xx} and ρ_{yy} models, divided into three layers of equal thickness: upper crust (0-25 km), lower crust (25-50 km), and upper mantle (50-75 km). The conductance of the lower crust beneath the Rocky Mountains is 1500-2000 Siemens (S). In comparison to other regions of our model, the LCC exhibits twice the conductance of the upper mantle directly beneath it, four times that of the Denver Basin (~500 Siemens), and an order of magnitude greater than that of the adjacent lower crust beneath the Great Plains. A lower-crustal conductance of 2000 S is extremely high for tectonically stable lower crust (averaging 40-400 S) [*Jones* 1992] but is modest compared to more tectonically active regions such as the Tibetan plateau (minimum 6000 S) [*Li et al*., 2003] and the East African Rift (~10 kS) [*Desissa et al*., 2013]. Given the well-resolved top of the LCC and assuming a uniform electrical resistivity for the entire lower crust yields a maximum average resistivity of 12-17 Ωm. Any vertically-varying distribution of lower crustal conductivity would thus require the existence of zones of much lower resistivity. Indeed if the observed lower-crustal conductance were confined to a layer 200 m thick within an otherwise resistive crust, the resistivity of that conductor would be only ~0.1 Ωm. Additional petrologic, geologic, and geophysical data are required to reasonably constrain the total thickness and conductivity of this anomaly.

The lower-crustal conductor exhibits the strongest degree of anisotropy (anisotropy factor of 2-3) of any feature in the top 75 km of the model (note separation of conductance curves in Figure 5b). Electrical resistivity in the lower crust appears to be enhanced in the x-direction (north-south, strike parallel) relative to the y-direction (east-west, strike perpendicular) (see Figures 4 and 5). Thus the electrical conductivity in the lower crust is enhanced in a direction parallel or sub-parallel to both the Rocky Mountain Front and the Rio Grande rift (Figure 1).

The anisotropic behavior we observe could be an artifact of the inversion produced by a series of north-south oriented elongate conductors with finite along strike length (i.e. quasi 3D conductive bodies parallel to strike). In this scenario, the segmented LCC shown in the isotropic model would be closer to the real Earth structure. We advocate instead for a bulk anisotropy as observed in Figure 4 based on the behavior of the tipper functions over the top of the conductor. The wavelength of the segmented conductors in Figure 3 is on the order of ~20 km. With nominal station spacing over the LCC of 5-10 km we should be able to resolve variability in the tipper due to the presence of strong lateral resistivity contrasts in the lower crust. Pseudo sections of Parkinson-convention tipper, especially the along profile component (Tzy) (Supplementary Material, Figure S5), show a binary distribution of induction vector orientations, with western stations pointing east and eastern stations pointing west, towards the interior of the LCC as expected for a laterally cohesive conductor.

3.4 Upper Mantle

The upper mantle in our anisotropic model is electrically conductive (< 30 Ωm) beneath the Rocky Mountains and increasingly resistive east of the Rocky Mountain Front. An eastward thickening wedge of resistive material extending from the base of the crust into the upper mantle (RM in Figure 4) characterizes the lateral transition from conductive to resistive mantle structure. This is in contrast to a similar lateral transition in the lower-crustal resistivity structure that is characterized by a sharp vertical contact located directly beneath the RMF. The gradual increase in upper-mantle resistivity to the east is also evident in Figure 5c, which shows gradually

decreasing upper-mantle conductance east of the RMF. The maximum resistivity observed in the upper mantle lies near the base of the crust on the eastern edge of our profile.

The lowest resistivity in the upper mantle is observed in the ρ_{yy} model directly beneath the Rocky Mountain Front (AC in Figure 4). While this anomaly appears in the model as an isolated body of low resistivity beneath the Front Range, it is possible that enhanced conductivity in the upper mantle extends to the west, beneath the lower-crustal conductor, and/or vertically down into the mantle directly beneath AC. The masking effects of the LCC and limited data coverage west of 106.25ºW make the lateral extent of this conductive anomaly difficult to resolve. Similarly, the high conductance of the feature limits our ability to resolve the depth to which it extends into the upper mantle. By ~150 km depth the upper mantle is conductive (< 30 Ωm) across the entire profile.

To first order, electrical resistivity structure below 150 km is characterized by subtle variations in resistivity, with a range of resistivity values spanning only half a decade in log-resistivity space (10-30 Ωm) over the entire model from 150-300 km depth. Lateral variations are practically non-existent and the overall trend is of decreasing resistivity with depth. If our data were sensitive to this type of resistivity structure, we would expect apparent resistivity of the off-diagonal impedance elements to decrease at long periods and for the corresponding phase at those periods to be increasing toward 90º. We do not observe these trends at most stations (e.g. Figure 2a) and where we do (e.g. Figure 2b) we prefer to attribute these effects to the large resistivity contrast in the uppermost mantle (i.e. 50-150 km depth) rather than a subtle resistivity gradient below 150 km. In an effort to limit our interpretation to the minimum structure required by the data, we therefore omit discussion of a possible vertical conductivity gradient in the mantle below 150 km.

4. Discussion

4.1 General Features

Important elements of the 2D anisotropic resistivity models shown in Figure 4 include: (1) a series of thin, near-surface conductors; (2) a crust that is broadly resistive with the exception of the LCC; (3) the lower-crustal conductor; and (4) the gradual transition from conductive to resistive upper mantle under the Great Plains. We will address the first two briefly before commenting on the lower-crustal conductor and mantle resistivity structure in greater detail. Figure 6 shows an interpretive view of the anisotropic resistivity model with labels corresponding to major features and subsequent interpretation.

The three near surface conductors (PB, SP, and DB in Figure 6) correlate with three deep sedimentary basins: the Piceance, South Park, and Denver Basins (Figure 1). The low resistivity observed in each of these basins is likely due to the presence of electrically conductive Mesozoic marine shales. These are the Mancos shale in the Piceance and South Park Basins and a correlating unit, the Pierre shale, in the Denver Basin [*Izett et al*., 1971; *Maughan* 1988]. While the conductivity-thickness trade off discussed above prevents us from directly measuring the thickness of these sedimentary basins using our 2D resistivity model, we can derive an estimate for thickness using observed conductance and in situ measurements of electrical resistivity of the geologic units found in these basins. For example, ground and airborne electromagnetic measurements of the Pierre shale in the Denver Basin show that it is electrically conductive, typically 3-8 Ωm [e.g. *Ackermann* 1974; *Abraham et al*., 2012]. Assuming that this unit is responsible for the majority of the upper-crustal conductance observed east of the Rocky Mountain Front (~500 S, see Figure 5), we calculate a thickness for the Pierre shale of 1500-

4000 m, which is consistent with previously published estimates for that particular unit in the Denver Basin (e.g. 2420 m, [*Porter and Weimar*, 1982]).

Excluding the lower crustal conductor and the sedimentary basins discussed above, the top 50 km of our anisotropic resistivity model exhibits conductance values of stable tectonic crust [*Jones* 1992]. The upper crust to the west, beneath the Rocky Mountain Front Range, appears to exhibit substantially greater resistivity (>1000 Ωm) than that of the Great Plains (100-300 Ωm). This contrast is likely in part due to the screening effect of the conductive Denver Basin masking higher resistivity values in the upper crust beneath the Great Plains. The near-surface conductor associated with the Denver Basin is much thicker than estimated depth to resistive basement [*Mooney and Kaban*, 2010], indicating vertical smearing of this conductor. There is no such screening effect observed for the Rocky Mountain Front Range, where resistive metamorphic and plutonic rocks outcrop at the surface. Previous geophysical studies suggest that the bulk composition of the shallow crust in the southern Rocky Mountains has been altered by repeated intrusion of high-volume silicic magma bodies in the late Cenozoic [*McCoy et al*., 2005; *Li et al*., 2002; *Decker et al*., 1988]. Our results do not contradict this interpretation. However, our results do suggest that there is no significant volume of fluid or partial melt in the upper crust today. A large volume of interconnected melt fraction or aqueous fluid in the upper crust would significantly reduce bulk resistivity, which we do not observe.

4.2 Lower Crustal Conductor

The presence of low resistivities in the lower crust and upper mantle is consistent with previous investigations into the electrical resistivity structure of the lithosphere in Colorado. Reitzal et al., [1970] present the results of a large scale geomagnetic deep-sounding (GDS) survey of the western United States and find two broad "ridges" of high conductivity in the uppermost mantle, one beneath the southern Rocky Mountains and Rio Grande Rift and the other along the Wasatch Front in Utah. Both anomalies are elongate in the north-south direction, parallel to the Rocky Mountain Front. Subsequent modeling of that same data by Porath [1970] yielded two quantitative models of upper mantle resistivity structure that confirmed that high conductivity shallows beneath the Rocky Mountains in Colorado. The techniques used in that study lacked the depth resolution to differentiate between models with high conductivities near the lithosphere-asthenosphere boundary at 150 km, and an alternate but equally well fitting model with high conductivity near the base of the crust at 45 km. Our results suggest that the model with a shallower conductor in the lower crust and uppermost mantle is the more likely scenario.

The mechanisms most often invoked for explaining low resistivities in the lower crust are highly conductive phases that form interconnected conduction pathways along grain boundaries, including sulfide minerals, graphite films, and fluids such as partial melt or saline brines [*Yang* 2011]. *Kariya and Shankland* [1983] show that the resistivity of crustal rocks may also decrease with increasing temperature, e.g. dry basaltic rocks decrease in resistivity from 10^4 to 20 Ωm from 500-1000ºC. Low seismic velocities in the upper mantle [e.g. *Shen and Ritzwoller*, 2016] and elevated crustal geotherms [*Decker et al*., 1988] suggest that upper-mantle and lower-crustal temperatures in some regions of the southern Rocky Mountains in Colorado may easily exceed 1000ºC. Could elevated crustal temperatures, essentially hot dry rock, produce the observed conductivity anomaly in the mid-to lower crust without the need for additional conductivity mechanisms?

425 **4.2.1 Solid-state Conductivity Mechanisms in the Lower Crust**

426 *Kariya and Shankland* [1983] compile results from a multitude of laboratory studies to
427 examine the effect of temperature on the bulk resistivity of dry, sub-solidus crustal rocks of both
428 mafic and felsic composition. They show that dry rocks of felsic and intermediate compositions
429 do not achieve resistivity values below ~2000 Ωm, even at elevated temperatures approaching
430 the solidus (~1000ºC). Basaltic rocks can achieve the resistivity required to explain the lower
431 crustal conductor ($\rho < 20$ Ωm), but only at or near the solidus. Adjusting for the effect of
432 pressure on the basalt dry solidus would theoretically allow the lower crust to achieve higher
433 temperatures (and thus lower resistivity) without melting (e.g. maximum temperature of 1200ºC
434 at 50 km depth). However, in order for elevated bulk temperature to account for the observed
435 lower crustal anomaly, the entire crust from 25 km depth to the crust-mantle interface would
436 need to be comprised of basalt at or above 1000ºC. Not only are mid-crustal temperatures
437 >1000ºC not supported by regional estimates of crustal geotherms [e.g. *Decker et al*., 1988],
438 several seismic tomography studies argue in favor of a predominantly felsic composition of the
439 lower crust west of the Rocky Mountain Front [e.g. *Li et al*., 2002; *Schmandt et al*., 2015]. We
440 conclude that if the lower crust is dry, variations in bulk temperature and composition are
441 insufficient to produce the observed conductivity anomaly without additional contributions from
442 grain-boundary conduction mechanisms.

443 Sulfide mineralization and thin graphite films can be exceptionally conductive and
444 produce significant low resistivity anomalies in otherwise cold and dry lower crust [e.g.
445 *Bedrosian and Box*, 2016; *Bedrosian* 2016; *Boerner et al*., 1996]. Thin graphite films form when
446 thick packages of carbon bearing sedimentary rocks, typically deposited in deep marine basins,
447 are subjected to intense heat and pressure, leading to the formation of graphite films along
448 metamorphic fabrics. Sulfide mineralization occurs by a similar process, involving large volumes
449 of sulfide-bearing sedimentary rocks, also typically sourced from deep marine depositional
450 environments. The presence of graphite or sulfide mineralization in the deep crust requires both a
451 geologic source of the appropriate minerals and a tectonic history that includes forces capable of
452 emplacing those minerals in the deep crust. There is no evidence to suggest that central Colorado
453 meets either of these requirements.

454 The most significant source of sulfide mineralization in Colorado is the "Colorado
455 Mineral Belt" (CMB) [*Tweto and Sims*, 1963], a collection of sulfide-bearing hydrothermal,
456 volcanic, and plutonic ore-bodies that form a northeast trending line from the southwest corner
457 of the state to near Boulder, Colorado. The CMB crosses our profile near 106ºW longitude, well
458 within the surface projection of the lower crustal conductor. However, the CMB is a relatively
459 narrow feature (~50 km wide at most) and the presence of sulfides near the surface does not
460 require the existence of large volumes of sulfide mineralization at depth. In terms of graphite
461 mineralization, there is no geologic evidence to suggest a large source volume of carbon-bearing
462 rocks exists in central Colorado.

463

464 **4.2.2 Partial Melt**

465 We consider saline fluids and partial melt the most likely sources of high conductivity in
466 the lower crust of the southern Rocky Mountains. The inherent non-uniqueness of the
467 magnetotelluric problem and the tendency for conductive bodies to smear vertically in
468 regularized inversion (e.g. Figure S3) make it difficult to differentiate between fluids and melt
469 with MT alone. We will use petrologic, geochemical, and additional geophysical evidence to
470 investigate the likelihood that the imaged conductor is partial melt, saline fluid, or a combination

of the two. Figure 7 provides a diagram of the various melt and fluid distributions that we consider below.

We first consider the end-member case in which the high conductivity of the lower crustal conductor is attributed solely to partial melt (Figure 7a and 7b). *Annen et al*. [2006] describe in detail the type of deep-crustal magma reservoir, or "lower crustal hot zone", that could produce the observed conductivity anomaly: Over a protracted period of time, basaltic magma is intermittently or continuously injected into the crust from the underlying mantle as horizontal sills. The basaltic melt then stalls in the mid- to lower crust either because it is of sufficient density to be neutrally buoyant or because it is sufficiently viscous due to a higher volatile content. The melt then cools and fractionates into more buoyant, andesitic melt that rises towards the surface, leaving behind a basalt residual. Small pipes of basaltic melt may also escape towards the surface [*Jacob et al*., 2015].

There is ample evidence to support the existence of this petrologic model at work in the southern Rocky Mountains in the very recent past. As stated previously, seismic tomography reveals the upper mantle directly beneath the Rocky Mountains to be anomalously warm [*Hansen et al*., 2015] and may contain melt that could be supplied to the lower crust [e.g. *Humphreys et al*., 2003]. The presence of melt in the crust would increase seismic attenuation and *Phillips et al*. [2014] observe that seismic attenuation of Lg surface waves at frequencies corresponding to crustal depths (0.75-1.5 Hz) is high for most of Colorado west of the Rocky Mountain Front. *Levandowski et al*. [2014] found that mapping seismic shear-wave velocity to density structure overestimates the buoyancy of the crust in central Colorado. They conclude that the presence of crustal melt could produce the observed effect, as partial melt would greatly reduce shear-wave speed without significantly altering bulk density. Geotherm estimates from *Decker et al*. [1988] suggest that the crust beneath the Rio Grande Rift in central Colorado (106.25ºW along our profile) resides above the basalt dry solidus at depths >36 km and above the alkali basalt saturated solidus at even shallower depths. Lastly, and perhaps most directly relevant, there is a collection of Quaternary age basalt flows in central Colorado, the youngest of which was erupted ~4,150 years before present [*Rowe et al*., 2015] near Dotsero, CO (blue star, Fig. 1). Geochemical analysis performed by *Leat et al*. [1989] suggest that the Dotsero magmas did experience at least a limited amount of fractional crystallization at pressures appropriate for the lower crust, suggesting these magmas are associated with a crustal magma reservoir.

Assuming that the elevated electrical conductivity observed in the mid- to lower-crust is the result of a distinct crustal zone containing some unknown melt fraction, we can constrain the physical and petrologic properties of that melt using the work of *Waff* [1974]. The bulk conductivity of a rock hosting partial melt is largely dependent on the electrical conductivity of the melt, the degree to which the melt is connected, and the fraction of the rock that contains partial melt. The contribution of the solid matrix resistivity to the bulk electrical properties of the rock is in most cases negligible. We will need to independently constrain most of these parameters if we are to extract a meaningful interpretation of the imaged MT anomaly.

We start by constraining the various parameters that control the conductivity of the melt. We utilize the online tool SIGMELTS [*Pommier and Le-Trong*, 2011] which uses a large database of experimental results and empirically-derived relationships to constrain the electrical conductivity of a melt based on a variety of physical and chemical parameters. More specifically, SIGMELTS provides a means for calculating silicate melt conductivity as a function of melt temperature, pressure, and composition (wt% H_2O, Na_2O, SiO_2). Partial melt is only electrically conductive so long as it is fluid, so presumably any melt observable by MT has a minimum

temperature above the solidus. The basalt dry solidus for depths of 25-50 km is 1160º-1200ºC. The solidus for wet basalt in the mid-crust is much lower, ~800ºC [*Decker et al*., 1988], due to the effect of water lowering the melting point. In the high temperature extreme we assume the melt has recently been extracted from the upper mantle. *Hansen et al*. [2015] map surface-wave shear velocities to lithospheric temperature for most of the U.S. and find a maximum temperature of ~1300ºC beneath central Colorado at a depth of 82 km. *Leat et al*. [1989] performed major element geochemistry for 14 rock samples collected from four Quaternary basalt flows in central Colorado, including the Dotsero flow. They found basalts high in sodium (wt% Na_2O = 3.74±0.34%) with silica values typical for basalt (wt% SiO_2 = 49.51±0.84%). Estimates of wt% H_2O for in situ partial melt are difficult to obtain but can be estimated via analysis of the volatiles present in fluid inclusions. For example, a recent study of late Cenozoic basalts erupted in northern New Mexico estimated the water content of the melt at 0.5-2.0 wt% H_2O [*Rowe et al*., 2015]. To our knowledge, no estimates of in situ water content exist for Quaternary magmas in Colorado, so we will consider the end-member cases of both dry and wet (2 wt% H_2O) basalt. Depth to the top of the conductor (25 km) provides an estimate of the minimum pressure experienced by the melt (~1 GPa). Passing these constraints through the SIGMELTS program yields melt conductivities of 0.6-1.5 S/m for dry basalt and 0.3-3.5 S/m for wet basalt, with the range of melt conductivity values encompassing the range of permissible temperature. Assuming a melt temperature of 1200ºC yields melt conductivities of 0.83 S/m and 1.78 S/m for dry and wet basalt, respectively.

Figure S6 shows the relationship between bulk resistivity of a rock and melt fraction contained within that rock for a melt of a particular conductivity, in this case 0.83 S/m (dry basalt) and 1.78 S/m (wet basalt). The geometrical model that forms the basis for this relationship (equation (26) in *Waff* [1974]) assumes a small melt fraction (<15%), a solid rock matrix that is substantially more resistive than the melt, and a 100% interconnected melt. Owing to the latter assumption, melt fraction estimates from this analysis are minimum values, as a less interconnected melt would require higher melt concentrations to produce the same bulk resistivity values. Because the physical constraints of the magnetotelluric method prohibit the independent determination of the thickness or absolute conductivity of the conductor (see Supplementary Material), our interpretation is subject to a tradeoff between bulk resistivity and melt fraction. In the extreme case that the melt is confined to a single tabular layer of molten rock, or a series of such layers containing nearly 100% melt (Figure 7a), the cumulative thickness of those melt layers would be 1.1 and 2.4 km for the wet and dry basalt, respectively. In the other extreme, where melt is distributed uniformly from 25 km depth to the base of the crust (Figure 7b), the melt fraction in the lower crust would be 7-15% for wet and dry basalt, respectively. We consider this a substantial melt fraction for a relatively amagmatic region of the continental interior. For comparison, *Desissa et al*. [2013] use magnetotelluric data and a similar analysis to estimate a melt fraction >13% for the crust beneath an incipient mid-ocean ridge in the Afar region of the East African Rift.

Basaltic underplating and/or injection of molten basalt into the mid-crust are expected to result in at least a limited degree of crustal melting. Relatively low seismic velocities in the deep crust [e.g. *Li et al.*, 2002] and a high magnitude density contrast across the crust-mantle boundary found by Schmandt et al. [2015] suggest that the deep crust beneath Colorado is of intermediate or felsic composition. If we alter the melt parameters in SIGMELTS to simulate the chemical composition of a typical rhyolite (~70% SiO_2, ~5% Na_2O) we find melt conductivities at 1200ºC of 0.09-0.44 S/m for dry and wet melts, respectively. Assuming a more felsic melt in

563 our interpretation would require a thicker melt layer and/or a higher melt fraction within the melt
564 zone. In interpreting the presence of melt in the lower crust we recognize that a spectrum of melt
565 compositions is likely present, including a felsic component contributed by anatectic melts,
566 especially given the inferred composition of the lower crust in Colorado. However, for the
567 purposes of putting meaningful constraints on melt fraction and melt layer thickness, we restrict
568 our interpretation to high conductivity melts (i.e. basaltic melts) as that assumption provides
569 minimum values of layer thickness and melt fraction well suited for hypothesis testing in
570 subsequent work.
571
572 **4.2.3 Aqueous Fluid**
573 Another likely source of high conductivity in the lower crust, especially in active tectonic
574 environments, is aqueous fluid [e.g. *Li et al*., 2003; *Wannamaker et al*., 2008]. Saline fluids in
575 the deep crust can easily exceed the conductivity of seawater (>3 S/m) and can produce high
576 conductivity anomalies with far smaller fluid volumes than required for anomalies of similar
577 conductance comprised of partial melt. Where it is available, seismic reflection data can be
578 helpful in differentiating aqueous fluid from partial melt in deep-crustal conductors. The
579 concentration of fluids into lenses produces high impedance contrast "bright spots" in seismic
580 reflection sections that are often coincident with lower-crustal conductors [*Hyndman and*
581 *Shearer*, 1989]. The Continental Dynamics of the Rocky Mountains (CD-ROM) experiment
582 included the acquisition of seismic refraction and reflection data along the crest of the southern
583 Rocky Mountains. At the latitude of our MT profile in central Colorado, *Rumpfhuber and Keller*
584 [2009] observe a mid-crustal reflector in the CD-ROM data at depths similar to the well-resolved
585 top of the lower crustal conductor (22-23 km). However, they suggest the reflector is a product
586 of the interwedging of crustal blocks from adjacent Proterozoic terranes, juxtaposed during the
587 assembly of the North American continent, and do not consider the role of fluids in their
588 interpretation.
589 Absent independent geologic and geophysical evidence for the presence of saline fluid in
590 the deep crust we rely on the results of laboratory studies and estimates of fluid porosity to assess
591 the likelihood that fluids contribute to the observed high conductivity. We do not consider the
592 scenario in which aqueous fluids permeate the entire lower crust. *Yardley and Valley* [1997]
593 argue that in stable tectonic regimes high-grade metamorphic and igneous rocks of the lower
594 crust will readily incorporate free fluids to produce hydrated retrograde metamorphic minerals
595 and that the lower crust in general behaves as a fluid-sink rather than a fluid-source. Even in
596 more active tectonic regimes it is difficult to maintain vertically distributed free fluids in the
597 lower crust. The permeability required to produce observable volumes of interconnected free
598 fluid in the lower crust would also facilitate the evacuation of that buoyant fluid to shallower
599 depths.
600 Figure 7c shows a typical model of fluid distribution that is often invoked to explain low
601 resistivity anomalies in the mid- to lower crust. In this model, saline fluids are typically
602 interpreted as thin horizons of accumulated fluid ponding beneath impermeable barriers to
603 upward fluid flow [e.g. *Hyndman and Shearer*, 1989; *Jiracek et al*., 1983; *Eaton* 1980]. *Eaton*
604 [1980] suggests that ductile shear concentrated near the brittle-ductile transition during
605 lithospheric extension may produce a pervasive physical barrier to fluid migration. Fluid flow at
606 mid-crustal levels may also be impeded by fluid-rock interactions that reduce permeability, such
607 as silicate precipitation and/or volume increasing hydration reactions [*Hyndman and Shearer*,
608 1989]. In the former scenario, the LCC indicates depth to the brittle-ductile transition and/or a

609 pervasive mid-crustal decollement associated with regional-scale crustal extension. In the latter,
610 the top of the LCC corresponds to the isotherm associated with silicate precipitation and
611 retrograde metamorphism reactions (350-400ºC). These interpretations are not mutually
612 exclusive.
613 *Shimojuku et al*. [2014] provide estimates of the bulk electrical conductivity of brine-
614 bearing quartzite under mid-crustal conditions (T = 800-1100 K, P = 1 GPa). The most
615 conductive sample tested (quartzite with 30% fluid fraction consisting of 17 wt% NaCl brine)
616 exhibited a bulk conductivity of ~4 S/m, with little variation due to temperature. A layer of
617 brine-bearing quartzite with this porosity and salinity would need to be just 500 m thick in order
618 to produce the observed lower crustal conductance of 2000 S. Extrapolating to a more modest
619 fluid fraction of 10%, based on examination of mid-crustal "bright spots" in Tibet [*Caldwell et*
620 *al*., 2009], yields a bulk conductivity of 1.25 S/m, which would require a layer of fluid-bearing
621 rock 1.6 km thick to produced the observed conductance. We consider this the minimum
622 thickness of a brine-bearing rock layer required to produce the observed high conductivity, as
623 thinner layers would require salinity and/or fluid fractions that may not be reasonable for the
624 depths at which high conductivity is observed. Lower salinity and/or porosity would require a
625 thicker layer of fluid accumulation and/or an increasingly high aggregate volume of mid-crustal
626 fluid.
627
628 **4.2.4 Preferred Geologic Model for the Lower Crust**
629 Figure 7d shows our preferred interpretation of the lower crustal conductor, in which both
630 partial melt and saline fluids are present. The end-member cases presented in the previous
631 sections and illustrated in Figure 7a-c are problematic in that they would not produce the
632 observed strike-parallel anisotropy. We appeal instead to a model in which melt is supplied to the
633 crust via melt-filled fractures, or vertical dikes, aligned parallel to strike. These melt-filled cracks
634 would produce the observed anisotropy by providing a north-south aligned fabric that would
635 preferentially channel electric currents into a strike-parallel direction. These fractures are either
636 sufficiently thin or too closely spaced so as to prevent our model from resolving individual
637 cracks. The north-south orientation of fractures is consistent with the inferred local stress regime.
638 Geodetic observations suggest that much of Colorado is experiencing distributed east-west
639 extension [*Berglund et al*., 2012], implying that the least principal stress direction is also
640 oriented east-west. Injection of magma into this type of stress regime would produce north-south
641 oriented dikes trending perpendicular to the least principal stress direction.
642 We cannot rule out the possibility that these strike-parallel fractures are alternatively or
643 simultaneously occupied by transient pulses of aqueous fluid. However, we find it difficult to
644 advocate for a model that does not include some fraction of partial melt. The fluid concentrations
645 required to produce the observed anomaly (up to 10%, see above) would reduce the solidus to
646 the point of melting the crust given the high temperatures modeled for the lower crust in the
647 region [*Decker et al.*, 1988]. Furthermore, the independent geophysical evidence for lower
648 crustal melt and Quaternary volcanism in Colorado described above suggest that a "water only"
649 model is unlikely.
650 Our preferred model also includes melt and aqueous fluid ponding at mid-crustal levels.
651 These features are added to explain the presence of the lower crustal conductor in the strike
652 perpendicular resistivity model (Figure 4b). These ponded fluids provide a component of
653 isotropic high conductivity at the top of the LCC resolvable in both components of the
654 anisotropic inversion results. Ponded melt is a straightforward consequence of supplying melt to

the lower crust, while ponded fluids are expected to result from crust-melt interactions. Possible sources of fluid in this scenario include magmatic fluid exsolving from the partial melt as it cools and metamorphic fluids released by heating of hydrous minerals in the surrounding crust.

4.3 Upper Mantle Resistivity Structure

Seismic tomography, teleseismic travel time residuals, and receiver function studies suggest a substantial increase in thickness of the sub-continental lithospheric mantle (SCLM) from west to east across the Rocky Mountain Front [e.g. *Sheehan et al*., 1995; *Lee and Grand*, 1996; *Yuan et al*., 2014; *Hansen et al*., 2015]. *Sheehan et al*., [1995], for example, advocate for a mantle density structure in which the high density lithospheric mantle lid is 60 km thicker under the Great Plains than it is under the adjacent Southern Rocky Mountains. Our preferred anisotropic electrical resistivity model shows a moderately resistive (>50 Ωm) eastward-thickening feature in the Great Plains upper mantle extending from the base of the crust to depths of 125-150 km beneath the eastern edge of our profile (RM in Figure 4). Does this transition from conductive to resistive upper mantle represent the electrical lithosphere-asthenosphere boundary (LAB) shallowing to the west? Or is it simply an alteration and/or thermal boundary internal to the mantle lithosphere?

4.3.1 Electrical lithosphere-asthenosphere boundary

We first consider the scenario in which the lateral resistivity structure imaged beneath the Great Plains within the top 150 km of our model reflects the electrical LAB shallowing towards the range front from the east. *Dai and Karato* [2009] cite typical resistivity values of 10-25 Ωm to calculate moderate bulk water content (100-400 ppm) for typical asthenosphere at `1300ºC. Figure 6 shows an approximate 30 Ωm resistivity contour in the upper mantle of our model east of the range front. If we assume that this contour represents the LAB, we would expect asthenospheric temperatures of >1200ºC, and consequently low seismic velocities, to be imaged east of the Rocky Mountain Front at depths <100 km.

Seismic tomography studies that utilize surface waves and/or ambient noise are in particular sensitive to seismic velocity structure over the depth range of the most pronounced features in our electrical resistivity models (near-surface to 150 km). A number of such studies have been performed across the RMF [*Li et al*., 2002; *Shen et al*., 2013; *Hansen et al*., 2015; *Shen and Ritzwoller* 2016]. *Li et al.* [2002], for example, provide a high lateral resolution image of upper mantle velocity perturbations along our profile that shows a sharp lateral contrast in upper mantle velocity structure across a vertical boundary located at ~105ºW that persists to depths >150 km (Figure 6d). This suggests that the mantle directly east of the range front is cold and likely not asthenosphere. However, more recent seismic tomography studies utilizing the USArray [*Shen and Ritzwoller,* 2016] and more focused studies using local seismic networks [*Hansen et al.*, 2013] produce conflicting results for model regions within 50-100 km of the Rocky Mountain Front (Figure S7). It is difficult to reconcile our magnetotelluric results with the differing seismic models. We note that all of these seismic studies lack the dense station distribution of the magnetotelluric study, in particular east of the range front, and those that exhibit the easternmost extent of low velocity out into the plains [e.g. *Shen and Ritzwoller*, 2016] also have the least dense station spacing (~70 km). The thick sedimentary package of the Denver Basin provides an additional complication in the modeling of seismic wave speeds adjacent to the range front and may account in part for the variability observed in the seismic results.

700 In the scenario in which we assume that we are successfully imaging the electrical LAB
701 east of the range front, the 30 Ωm contour is the minimum depth to that boundary. In reality, the
702 depth to the LAB is likely much deeper than the 30 Ωm contour, especially near the range front
703 where the contour impinges on the base of the crust. We expect that a buffer of lithospheric
704 material of likely indeterminable thickness is present at the base of the crust across our entire
705 profile. Under this assumption, we still must account for the relatively high conductivity (30-100
706 Ωm) present east of the RMF above the 30 Ωm contour and below the resistive crust, a region of
707 what is most likely sub-continental lithospheric mantle.
708
709 **4.3.1 Modification of sub-continental lithospheric mantle**
710 To further examine the distribution of lithospheric mantle material beneath the Great
711 Plains, and to better characterize the physical and chemical state of said lithosphere, we examine
712 typical resistivity values of continental lithospheric mantle under various conditions. Electrical
713 conductivity of the lithospheric mantle may be enhanced by the presence of partial melt, water in
714 nominally anhydrous minerals, and to a lesser extent, elevated bulk temperature. Using the
715 unified olivine conductivity model of *Gardes et al*., [2014] we estimate that even at
716 exceptionally high temperatures (>1300ºC), the resistivity of the mantle lithosphere cannot
717 achieve resistivity values below ~100 Ωm without the addition of melt and/or hydration. We note
718 that the conductivity model of Gardes et al. is limited to olivine conductivity; however, we do
719 not expect more complex mantle lithologies (e.g. including pyroxenes and garnet) to exhibit
720 substantially higher conductivity under dry conditions. We have plotted an approximate 100 Ωm
721 contour for the upper mantle east of the RMF in Figure 6. In our interpretation, this contour
722 represents the maximum depth to which the lithospheric mantle beneath the plains may be dry
723 and/or melt-free. The resistivity values observed below the 100 Ωm contour are incompatible
724 with unmodified SCLM. Although the 100 Ωm contour represents a minimum threshold for dry
725 conditions, we expect that modification also extends above this line given that seismic estimates
726 of upper mantle temperature at these depths [~1000ºC, *Hansen et al*., 2015] are still too low to
727 account for observed resistivity < 10^3 Ωm [*Constable et al*., 1992].
728 Estimates of dissolved water content of the lithospheric mantle beneath the Great Plains
729 are constrained by the analysis represented in Figure 8. This figure was inspired by a similar
730 analysis performed by *Bedrosian* [2016] to assess hydration of the SCLM beneath the
731 Midwestern United States. Figure 8a shows several resistivity vs. depth profiles for the Great
732 Plains upper mantle taken from the 2D resistivity model in Figure 4a. Vertical resistivity profiles
733 are extracted from a region of the model extending laterally from just east of the RMF to the
734 eastern edge of the model near the Colorado-Kansas border. The resistivity model was sampled
735 at an interval of ~20 km. For comparison, the model profiles have been plotted together with
736 resistivity-depth profiles calculated using a model for olivine resistivity as a function of
737 dissolved water content and temperature [*Gardes et al*., 2014]. We assume a conductive mantle
738 geotherm for the region, accounting for variable heat production and a surface heat flow of 40-80
739 mW/m^2 [*Hasterok and Chapman*, 2011], with the different resistivity models in Figure 8a
740 representing results obtained assuming the various geotherms shown in Figure 8b. Note that the
741 geotherms converge to a mantle adiabat with potential temperature of 1400ºC. Models for
742 anhydrous and hydrous (100 ppm H_2O) olivine are shown. Also plotted in Figure 8b are the dry
743 peridotite solidus [orange line, *Hirschmann* 2000], the saturated peridotite solidus [purple line,
744 *Till et al*., 2010]., and two seismically derived estimates of upper mantle temperature in eastern
745 Colorado from *Hansen et al*. [2015] and *Schutt et al*. [2012].

We can draw several conclusions about the physical state of the lithosphere east of the Rocky Mountain Front from examination of Figure 8. The primary observation is that the modeled electrical resistivity is predominantly inconsistent with a dry lithospheric mantle. The "water free" olivine resistivity model (gray lines, Figure 8a) only approaches the model resistivity profiles for the easternmost profiles assuming the highest geothermal gradients. Surface heat flow actually decreases with distance east of the range front and near the Colorado-Kansas border is well below the 70-80 mW/m^2 values that would be indicative of the thermal regime required to produce the observed resistivity in the mantle lithosphere. If we assume that partial melting of dry lithosphere were contributing to the low resistivity, we would expect the geothermal gradient to exceed the peridotite dry solidus over a significant depth range coincident with the observed low resistivity. This is not the case for even the warmest lithospheric temperature profile (Figure 8b). Thus our preferred electrical resistivity model is incompatible with a "water free" mantle lithosphere beneath the Great Plains, at least to the eastern extent of our profile.

We observe two clear patterns in the resistivity profiles from our anisotropic model: (1) the average bulk resistivity of the upper mantle increases from west to east and (2) the depth to the minimum resistivity increases along the same trend, i.e. the profiles becomes steeper towards Kansas. If we interpret the first trend in terms of water content, the implication is that dissolved water concentration in the mantle increases towards the range front, with maximum hydration occurring beneath the RMF. The second trend, a steepening of the resistivity profile, is consistent with the behavior observed for a decrease in geothermal gradient, or thickening of the lithosphere. That we observe steepening of the profiles from west to east suggests that the lithosphere may be thickening to the east. We emphasize, however, that the resistivity values throughout the model are too low for variations in lithospheric thickness to fully account for conductivity increasing towards the range front.

We consider the qualitative observation of a hydrated lithosphere east of the Rocky Mountain Front to be our most important finding with regard to upper mantle resistivity structure. The observation of a gradual change in resistivity structure beneath the plains is equally significant in that it suggests that RMF transition zone in not as abrupt in the mantle lithosphere as it may be in the crust. The following attempts to further quantify the amount of water dissolved in the upper mantle are presented to confirm that hydration is a reasonable interpretation and aid in future hypothesis testing.

We observe from Figure 8a that the resistivity profiles derived from the MT results fit an olivine resistivity model with water content of 100 ppm much better than that of anhydrous olivine. While hydrous olivine may be responsible for the majority of high conductivity in the upper mantle, estimates of bulk mantle water content and subsequent assessment of whether those estimates are reasonable must take into consideration other nominally anhydrous minerals. We can use the method of *Sarafian et al*., [2015] to convert mantle olivine water content into bulk mantle water content based on modal proportions of peridotite minerals and partition coefficients. Assuming 100 ppm water in olivine and a pyrolite composition of olivine:orthopyroxene:garent = 60:25:15 yields a bulk mantle water content >400 ppm or >0.04 wt% H_2O. This value is relatively high but not unreasonable compared to other magnetotelluric determinations of lithospheric water content [e.g. 10^{-2} wt% Selway et al., 2014].

Partial melt may also contribute to the high conductivity beneath the westernmost Great Plains. There is no direct evidence from seismic tomography [e.g. *Li et al*., 2002, Figure 6d], body-wave attenuation [*Boyd and Sheehan*, 2005], seismicity [*Nakai et al*., 2017], surface

792 geology, or heat flow to suggest that there are any active or recently active magmatic systems
793 beneath the Great Plains in eastern Colorado at this latitude. However, plotting the saturated
794 peridotite solidus [*Till et al*., 2010], along with reasonable estimates of continental geotherms for
795 this region (Figure 8b) shows that conditions in the upper mantle may permit partial melting of
796 hydrous peridotite. We speculate that partial melt beneath the western plains could represent a
797 possible reservoir or melt pathway for the partial melt present in the lower crustal conductor.
798 Indeed, the anisotropic (east-west conductive) anomaly AC in Figure 4b may reflect the lateral
799 transport of the proposed melt.
800
801 **4.3.3 Upper mantle structure west of the RMF**
802 We limit our discussion of the upper-mantle resistivity structure west of the Rocky
803 Mountain Front to a few broad observations, given that screening effects of the lower-crustal
804 conductor severely limit our ability to resolve mantle structure and the resistivity contrasts in the
805 mantle below it are expected to be slight. The upper mantle beneath the southern Rocky
806 Mountains appears to be generally conductive (~30 Ωm) and isotropic (Figure 5c). Seismic
807 tomography and receiver function studies indicate that the lithosphere-asthenosphere boundary is
808 relatively shallow beneath the southern Rocky Mountains, perhaps at depths <90 km [e.g.
809 *Sheehan et al.,* 1995]. The resistivity values observed beneath the LCC at those depths are
810 consistent with modeled asthenospheric resistivity (30 Ωm for 100 ppm H_2O asthenosphere, *Dai*
811 *and Karato*, [2009]). However, lithospheric mantle that has been hydrated and/or infiltrated by
812 partial melt, as suggested, for example, by *Humphreys et al*. [2003], is expected to exhibit
813 similarly low resistivity values. This lithospheric stratigraphy is in contrast to that of the more
814 energetic Snake River Plain magmatic region near Yellowstone, which exhibits resistivity values
815 in the upper mantle consistent with dry lithosphere [*Meqbel et al*., 2014]. The low resistivity
816 lithosphere beneath the southern Rocky Mountains suggests that melt and/or fluids persist in the
817 upper mantle and remain to be fluxed through this less active magmatic system.
818 Thinned lithosphere beneath the SRM is a plausible explanation for the observed
819 resistivity structure, although it is unlikely that we can independently constrain lithospheric
820 thickness in this portion of the model. Petrologic and geophysical evidence suggests that
821 lithospheric stratigraphy beneath the southern Rocky Mountains in Colorado consists of heavily
822 modified lower crust [this study], hot and/or partially molten mantle lithosphere [e.g. *Humphreys*
823 *et al.,* 2003], and hydrous asthenosphere, none of which is expected to be resistive. Determining
824 lithospheric thickness in this type of tectonic environment (i.e. imaging the boundary between
825 two conductive layers of the upper mantle) would be difficult even without the masking effects
826 of the LCC. In terms of upper mantle structure beneath the LCC, we appeal to the existing
827 interpretations from the seismic community (i.e. thinned lithosphere) and note that our data does
828 nothing to refute that hypothesis.
829
830 **4.4 Tectonic Implications**
831 **4.4.1 Partial melt in the lower crust**
832 In interpreting the lower crustal conductor we must consider the timing of fluid
833 emplacement, the source of fluids, and the spatial scale of the anomaly. Partial melt emplaced in
834 the mid-crust is not at thermal equilibrium with the surrounding rock and will freeze over several
835 thousands to millions of years, depending on the volume and frequency of repeated injection and
836 initial crustal temperature [*Annen et al*., 2006]. *Yardley and Valley* [2000] argue that saline
837 brines in the lower crust can only persist as free fluids for a limited geologic time before the

chemical, thermal, and pressure conditions of the lower crust that favor hydration reactions will consume those fluids in retrograde metamorphism. The width of the lower crustal resistivity anomaly dictates that any mechanism we invoke for supplying fluids to the lower crust must be capable of producing laterally pervasive crustal modification. The high conductivity that we image is therefore the result of recent tectonic activity that has provided volatiles, heat, and/or magma to a broad area of the lower crust in the very recent past and/or in a sustained manner over the last few million years.

It is reasonable to assume that the partial melt that we interpret to exist in the mid- to lower crust is the result of melting of the lithosphere. *Humphreys et al*., [2003] argue that low seismic velocity in the upper mantle beneath the southern Rocky Mountains represents hot, dry, and perhaps partially molten lithospheric mantle. *Leat et al*. [1989] advocate for a lithospheric mantle source for the Quaternary lavas erupted in central Colorado. Lithospheric melting is achieved through three mechanisms: the addition of heat, the addition of volatiles, and/or decompression melting. The first two mechanisms may also supply free fluids to the lower crust, either as exsolved magmatic fluids or fluids released from high-temperature metamorphic reactions of previously hydrated minerals.

Small-scale convection of the upper mantle is one plausible mechanism for melting the mantle lithosphere. The advection of heat, volatiles, and/or partially molten asthenosphere to the base of the lithosphere could all contribute to partial melting of lithospheric mantle. Geodynamic modeling by *van Wijk et al*. [2010] suggests small-scale edge-driven convection can initiate at a step in lithospheric thickness. They suggest this process is in part responsible for initiation of the Rio Grande Rift at the boundary between the Colorado Plateau and Great Plains in New Mexico, where the Great Plains crust and lithosphere is much thicker than that of the Colorado Plateau today [*Wilson et al*., 2005]. Section 4.3 describes the evidence for a differential lithospheric thickness across the Rocky Mountain Front in Colorado that could be responsible for the initiation of edge-driven convection in the sub-lithospheric mantle.

Determining the mechanism responsible for the initiation and continuation of small-scale convection beneath Colorado, or otherwise supplying melt to the lower crust, is left for future geodynamic modeling studies. We speculate, based on modest estimates of Cenozoic extension at the surface, that there are processes at work other than rifting, unless the mantle lithosphere has become substantially decoupled from the overlying crust. A mechanically destabilized lower crust could provide another means of initiating convection. The presence of water in the lower crust, especially at volumes suggested by the water rich end-member case discussed above (Figure 7c), could weaken and destabilize the crust [e.g. *Jackson et al*., 2004]. If the lower crust is also anti-buoyant, for example after basaltic underplating has densified the crust-mantle interface, one could imagine a scenario in which foundering of lithosphere into a shallow asthenosphere could generate decompression melting.

Electrical conductivity of the upper mantle is enhanced directly beneath the RMF (AC in Figure 4b, arrow in Figure 6). This anomaly appears to be anisotropic as well, with conductivity enhanced in the east-west direction, perpendicular to geoelectric strike (Figure 6c). We speculate that this resistivity structure reflects a flux of partial melt and fluids into the mantle lithosphere from an east-west directed convection cell upwelling beneath the Rocky Mountain Front transition zone. The 200 km width of the lower-crustal conductor may represent some characteristic length scale of this inferred convection cell, wherein melt and fluids flux out of the sub-lithospheric mantle as material moves from east to west, ultimately down welling beneath western Colorado.

884
885 **4.4.2 Hydration of the lithospheric mantle**
886 The possible identification of pervasive hydration of the lithospheric mantle east of the
887 Rocky Mountain Front has implications for the tectonic evolution and modification history of the
888 continental interior. An apparent eastward decrease in the degree of modification to the SCLM is
889 consistent with progressive dewatering during subduction of the eastward-dipping Farallon slab.
890 A similar mechanism for supplying water to the mantle has been proposed for more active
891 tectonic regions to the west [e.g. *Humphreys et al*., 2003] and has been invoked to explain
892 kimberlite eruptions in eastern Kansas in the late Cretaceous [*Currie and Beaumont*, 2011]. It is
893 difficult to constrain the hydration state east of the range front due to (1) a low availability of
894 extrusive volcanism to provide direct sampling of lithospheric mineralogy and water content and
895 (2) the minor H_2O concentration in nominally anhydrous minerals has a negligible effect on bulk
896 density and seismic velocity. The penetration of hydrous phases into the uppermost mantle has
897 implications for the ability of water to migrate through the lithosphere and may help explain the
898 presence of hydrated mineral phases in lower-crustal rocks above relatively thick lithosphere
899 [*Jones et al*., 2015]. One interpretation of the so-called "ignimbrite flare up" [*Lipman* 1992] is
900 that pervasive mantle hydration and refrigeration provided by the Farallon slab primed the
901 lithospheric mantle for melting upon slab removal and exposure to high temperature
902 asthenosphere. The reason the hydrated western plains did not follow a similar volcanic
903 progression is unclear, although our results show that hydrous partial melt may reside in the
904 Great Plains lithosphere today.
905
906 **5. Conclusions**
907 We present a 2D anisotropic electrical resistivity model of the crust and upper mantle
908 beneath the southern Rocky Mountains and Great Plains. We identify two significant features
909 that have implications for the tectonic evolution of the boundary between stable Proterozoic
910 lithosphere of the western Great Plains and recently modified lithosphere of the southern Rocky
911 Mountains: (1) a broad zone (200 km wide) of low resistivity (<20 Ωm) located at 25 km depth
912 beneath the highest topography in Colorado and (2) lower than expected resistivity in the upper
913 mantle east of the range front that we interpret as an eastward deepening "hydration front"
914 extending into the lithospheric mantle beneath the Great Plains. Interpreting the lower-crustal
915 conductor in the context of petrologic and geophysical constrains, we eliminate temperature,
916 composition, graphite and sulfide mineralization as the primary source of high conductivity. End
917 member petrologic models that may explain the high conductivity include ubiquitous basaltic
918 melt in the mid- to lower crust (7-15% melt fraction), a several kilometer thick sequence of
919 mafic sills recently injected into the mid-crust, and an accumulation of saline fluid ponding at the
920 brittle-ductile transition. The reality is likely some combination of these readily quantifiable end
921 member scenarios involving both saline fluids and partial melt (Figure 7d), such as north-south
922 oriented magmatic dikes that periodically supply basaltic magma and exsolved magmatic fluids
923 to mid-crustal levels. We speculate that basaltic magma in the lower crust beneath the Rocky
924 Mountains is the result of partial melting of the lithospheric mantle driven by the addition of heat
925 and/or volatiles from below. The existence of partial melt in the lower crust indicates that the
926 southern Rocky Mountains remain tectonically active. We speculate that edge-driven convection
927 initiated along a step in lithospheric thickness may play a significant role in driving that tectonic
928 activity. The increase in upper-mantle conductivity with depth beneath the Great Plains likely
929 represents a modification gradient internal to the sub-continental lithospheric mantle, although a

westward thinning lithosphere may also be observed. Hydration of the SCLM beneath the plains, possibly accomplished by dewatering of the shallowly subducting Farallon slab in the early Cenozoic, has implications for the tectonic evolution of the continental interior worthy of further investigation.

Acknowledgments

The authors thank the editor and an anonymous reviewer for constructive comments and suggestions. The authors thank Craig Jones, Lang Farmer, Peter Molnar, and Ned Sterne for valuable discussions. We thank Kerry Key and the Seafloor Electromagnetic Methods Consortium for the use of MARE2DEM and advice on its use. Our magnetotelluric data were collected over two summer field campaigns through a joint effort by the United States Geological Survey and the University of Colorado Boulder. Instrumentation was provided by the United States Geological Survey in Denver, CO and by Martyn Unsworth at the University of Alberta. This work was supported by the University of Colorado Boulder Geological Sciences Department Spetzler and W.O. Thompson awards, the Rocky Mountain Association of Geologists Bolyard Scholarship, the Society of Exploration Geophysicists, the Geological Society of America, and National Science Foundation grants EAR-1249669 and EAR-1053596. Additional support was provided by EarthScope (EAR-0323309). This work would not have been possible without land access granted by the National Forest Service, the State of Colorado, James Mark Jones State Wildlife Area, Douglas County Colorado, and numerous private landowners. Various maps and graphics were created using Generic Mapping Tools [*Wessel and Smith*, 1991]. Magnetotelluric transfer function estimates and time series used in this analysis are available through a US Geological Survey data release hosted on ScienceBase [https://doi.org/10.5066/F7610XTR].

References

Abraham, J. D., Cannia, J. C., Bedrosian, P. A., Johnson, M. R., Ball, L. B., & Sibray, S. S. (2012), Airborne electromagnetic mapping of the base of aquifer in areas of western Nebraska: U.S. Geological Survey Scientific Investigations Report 2011-5219.

Ackermann, H. D. (1974), Shallow seismic compressional and shear wave refraction and electrical resistivity investigations at Rocky Flats, Jefferson County, Colorado. Journal of Research of the U.S. Geological Survey, 2(4), 421–430.

Annen, C., Blundy, J. D., & Sparks, R. S. J. (2005), The Genesis of Intermediate and Silicic Magmas in Deep Crustal Hot Zones. Journal of Petrology, 47(3), 505–539, doi:10.1093/petrology/egi084

Bedrosian, P. A. (2016), Making it and breaking it in the Midwest: Continental assembly and rifting from modeling of EarthScope magnetotelluric data. Precambrian Research, 278, 337–361, doi:10.1016/j.precamres.2016.03.009

Bedrosian, P. A., & Box, S. E. (2016), Highly conductive horizons in the Mesoproterozoic Belt-Purcell Basin: Sulfidic early basin strata as key markers of Cordilleran shortening and Eocene extension. In J. S. MacLean & J. W. Sears (Eds.), Belt Basin: Window to Mesoproterozoic Earth: Geological Society of America Special Paper 522 (pp. 305–339), doi:10.1130/2016.2522(12).

Berglund, H. T., Sheehan, A. F., Murray, M. H., Roy, M., Lowry, A. R., Nerem, R. S., & Blume, F. (2012), Distributed deformation across the Rio Grande Rift, Great Plains, and Colorado Plateau. Geology, 40(1), 23–26, doi:10.1130/G32418.1

974 Boerner, D. E., Kurtz, R. D., & Craven, J. A. (1996), Electrical conductivity and Paleo-
975 Proterozoic foredeeps. Journal of Geophysical Research, 101(B6), 13775–13791,
976 doi:10.1029/96JB00171.
977 Booker, J. R. (2014), The Magnetotelluric Phase Tensor : A Critical Review. Surveys in
978 Geophysics, 35, 7–40, doi:10.1007/s10712-013-9234-2.
979 Boyd, O. S., & Sheehan, A. F. (2005), Attenuation Tomography Beneath the Rocky Mountain
980 Front: Implications for the Physical State of the Upper Mantle. In The Rocky Mountain
981 Region: An Evolving Lithosphere (pp. 361–377), Washington D.C.: American Geophysical
982 Union.
983 Caldwell, T. G., Bibby, H. M., & Brown, C. (2004), The magnetotelluric phase tensor.
984 Geophysical Journal International, 158, 457–469, doi:10.1111/j.1365-246X.2004.02281.x.
985 Caldwell, W. B., Klemperer, S. L., Rai, S. S., & Lawrence, J. F. (2009), Tectonophysics Partial
986 melt in the upper-middle crust of the northwest Himalaya revealed by Rayleigh wave
987 dispersion. Tectonophysics, 477, 58–65, doi:10.1016/j.tecto.2009.01.013.
988 Chapin, C. E., & Cather, S. M. (1994), Tectonic setting of the axial basins of the northern and
989 central Rio Grande rift. In G. R. Keller & S. M. Cather (Eds.), Basins of the Rio Grande
990 Rift: Structure, Stratigraphy, and Tectonic Setting: Geological Society of America Special
991 Paper (Vol. 291, pp. 5–26), Boulder, Colorado, doi:10.1130/SPE291-p5.
992 Constable, S. C., Parker, R. L., & Constable, C. G. (1987), Occam's inversion: A practical
993 algorithm for generating smooth models from electromagnetic sounding data. Geophysics,
994 52(3), 289–300.
995 Constable, S., Shankland, T. J., & Duba, A. (1992), The Electrical Conductivity of an Isotropic
996 Olivine Mantle. Journal of Geophysical Research, 97(B3), 3397–3404,
997 doi:10.1029/91JB02453.
998 Currie, C. A., & Beaumont, C. (2011), Are diamond-bearing Cretaceous kimberlites related to
999 low-angle subduction beneath western North America?, Earth and Planetary Science
1000 Letters, 303, 59-70.
1001 Dai, L., & Karato, S. (2009), Electrical conductivity of orthopyroxene: Implications for the water
1002 content of the asthenosphere. Proc. Jpn. Acad. Ser., 85, 466–475, doi:10.2183/pjab.85.466.
1003 DeCelles, P. G. (2004), Late Jurassic to Eocene evolution of the Cordilleran thrust belt and
1004 foreland basin system, western U.S.A. American Journal of Science, 304, 105–168.
1005 Decker, E. R., Heasler, H. P., Buelow, K. L., Baker, K. H., & Hallin, J. S. (1988), Significance of
1006 past and recent heat-flow and radioactivity studies in the Southern Rocky Mountains region.
1007 Geological Society of America Bulletin, 100, 1851–1885.
1008 Desissa, M., Johnson, N. E., Whaler, K. A., Hautot, S., Fisseha, S., & Dawes, G. J. K. (2013), A
1009 mantle magma reservoir beneath an incipient mid-ocean ridge in Afar, Ethiopia. Nature
1010 Geoscience, 6, 861–865, doi:10.1038/ngeo1925.
1011 Dickinson, W. R., Klute, M. A., Hayes, M. J., Janecke, S. U., Lundin, E. R., McKittrick, M. A.,
1012 & Olivares, M. D. (1988), Paleogeographic and paleotectonic setting of Laramide
1013 sedimentary basins in the central Rocky Mountain region. Geological Society of America
1014 Bulletin, 100, 1023–1039.
1015 Eaton, G. P. (1980), Geophysical and geological characteristics of the crust of the Basin and
1016 Range province. In Studies in Geophysics-Continental Tectonics (pp. 96–113), Washington
1017 D.C.: National Academy of Science.
1018 Eaton, G. P. (1987), Topography and origin of the southern Rocky Mountains and Alvarado
1019 Ridge. In M. P. Coward, J. F. Dewey, & P. L. Hancock (Eds.), Continental Extensional

Tectonics, Geological Society Special Publication (Vol. 28, pp. 355–369), Geological Society.

Eaton, G. P. (2008), Epeirogeny in the Southern Rocky Mountains region: Evidence and origin. Geosphere, 4(5), 764–784, doi:10.1130/GES00149.1.

Egbert, G. D. (1997), Robust multiple-station magnetotelluric data processing. Geophysical Journal International, 130, 475–496.

Epis, R. C., & Chapin, C. E. (1975), Geomorphic and Tectonic Implications of the Post-Laramide, Late Eocene Erosion Surface in the Southern Rocky Mountains. Geological Society of America Memoir, 144, 45–74.

Fenneman, N. M. (1946), Physical divisions of the United States.

Gamble, T. D., Goubau, W. M., & Clarke, J. (1979), Magnetotellurics with a remote magnetic reference. Geophysics, 44(1), 53–68.

Gardes, E., Gaillard, F., & Tarits, P. (2014), Toward a unified hydrous olivine electrical conductivity law. Geochemistry, Geophysics, Geosystems, 15, 4984–5000, doi:10.1002/2014GC005496.

Gilbert, H. (2012), Crustal structure and signatures of recent tectonism as influenced by ancient terranes in the western United States. Geopshere, 8(1), 141–157, doi:10.1130/GES00720.1.

Hansen, S. M., Dueker, K. G., Stachnik, J. C., Aster, R. C., & Karlstrom, K. E. (2013), A rootless rockies - Support and lithospheric structure of the Colorado Rocky Mountains inferred from CREST and TA seismic data. Geochemistry, Geophysics, Geosystems, 14(8), 2670–2695, doi:10.1002/ggge.20143.

Hansen, S. M., Dueker, K., & Schmandt, B. (2015), Thermal classification of lithospheric discontinuities beneath USArray. Earth and Planetary Science Letters, 431, 36–47, doi:10.1016/j.epsl.2015.09.009.

Hasterok, D., & Chapman, D. S. (2011), Heat production and geotherms for the continental lithosphere. Earth and Planetary Science Letters, 307, 59–70, doi:10.1016/j.epsl.2011.04.034.

Heise, W., & Pous, J. (2001), Effects of anisotropy on the two-dimensional inversion procedure. Geophysical Journal International, 147, 610–621.

Hirschmann, M. M. (2000), Mantle solidus: experimental constraints and the effects of peridotite composition. Geochem. Geophys, Geosyst. 1 (10).

Humphreys, E., Hessler, E., Dueker, K., Farmer, G. L., Erslev, E., & Atwater, T. (2003), How Laramide-Age Hydration of North American Lithosphere by the Farallon Slab Controlled Subsequent Activity in the Western United States. International Geology Review, 45(7), 575–595, doi:10.2747/0020-6814.45.7.575.

Hyndman, R. D., & Shearer, P. M. (1989), Water in the lower continental crust: modelling magnetotelluric and seismic reflection results. Geophysical Journal International, (98), 343–365.

Izett, G. A., Cobban, W. A., & Gill, J. R. (1971), The Pierre Shale Near Kremmling, Colorado, And Its Correlation to The East and the West: Geological Survey Professional Paper 684-A.

Jackson, J. A., Austrheim, H., McKenzie, D., & Priestley, K. (2004), Metastability, mechanical strength, and the support of mountain belts. Geology, 32, 625-628, doi:10.1130/G20397.1.

Jacob, K. H., Farmer, G. L., Buchwaldt, R., & Bowring, S. A. (2015), Deep crustal anatexis, magma mixing, and the generation of epizonal plutons in the Southern Rocky Mountains, Colorado. Contributions to Mineralogy and Petrology, 169(7), 1–23, doi:10.1007/s00410-014-1094-3.

1066 Jiracek, G. R., Gustafson, E. P., & Mitchell, P. S. (1983), Magnetotelluric results opposing
1067 magma origin of crustal conductors in the Rio Grande Rift. Tectonophysics, 94, 299–326.
1068 Jones, A. G. (1992), Electrical conductivity of the continental lower crust. In D. M. Fountain, R.
1069 J. Arculus, & R. W. Kay (Eds.), Continental Lower Crust (pp. 81–143), Elsevier.
1070 Jones, C. H., Mahan, K. H., Butcher, L. A., Levandowski, W. B., & Farmer, G. L. (2015),
1071 Continental uplift through crustal hydration. Geology, 43(4), 355–358,
1072 doi:10.1130/G36509.1.
1073 Kariya, K. A., & Shankland, T. J. (1983), Electrical conductivity of dry lower crustal rocks.
1074 Geophysics, 48(1), 52–61.
1075 Key, K. (2016), MARE2DEM: a 2-D inversion code for controlled-source electromagnetic and
1076 magnetotelluric data. Geophysical Journal International, 207, 571–588,
1077 doi:10.1093/gji/ggw290.
1078 Key, K., & Ovall, J. (2011), A parallel goal-oriented adaptive finite element method for 2.5-D
1079 electromagnetic modelling. Geophysical Journal International, 186, 137–154,
1080 doi:10.1111/j.1365-246X.2011.05025.x.
1081 Landman, R. L., & Flowers, R. M. (2013), (U-Th)/He thermochronologic constraints on the
1082 evolution of the northern Rio Grande Rift, Gore Range, Colorado, and implications for rift
1083 propagation models. Geosphere, 9(1), doi:10.1130/GES00826.1.
1084 Leat, P. T., Thompson, R. N., Dickin, A. P., Morrison, M. A., & Hendry, G. L. (1989),
1085 Quaternary volcanism in northwestern Colorado: Implications for the roles of asthenosphere
1086 and lithosphere in the genesis of continental basalts. Journal of Volcanology and
1087 Geothermal Research, 37, 291–310.
1088 Lee, D., & Grand, S. P. (1996), Upper mantle shear structure beneath the Colorado Rocky
1089 Mountains. Journal of Geophysical Research, 101(B10), 22233–22244.
1090 Levandowski, W. B., Jones, C. H., Shen, W., Ritzwoller, M. H., & Schulte-Pelkum, V. (2014),
1091 Origins of topography in the western U.S.: Mapping crustal and upper mantle density
1092 variations using a uniform seismic velocity model. Journal of Geophysical Research: Solid
1093 Earth, 119, 2375–2396, doi:10.1002/2013JB010607.
1094 Li, A., Forsyth, D. W., & Fischer, K. M. (2002), Evidence for shallow isostatic compensation of
1095 the southern Rocky Mountains from Rayleigh wave tomography. Geology, 30(8), 683–686.
1096 Li, S., Unsworth, M. J., Booker, J. R., Wei, W., Tan, H., & Jones, A. G. (2003), Partial melt or
1097 aqueous fluid in the mid-crust of Southern Tibet? Constraints from INDEPTH
1098 magnetotelluric data. Geophysical Journal International, 153, 289–304.
1099 Lipman, P. W. (1992), Magmatism in the Cordilleran United States; Progress and problems. In
1100 B. C. Burchfiel, P. W. Lipman, & M. L. Zoback (Eds.), The Geology of North America,
1101 The Cordilleran Orogen: Conterminous U.S. (pp. 481–514), Boulder, Colorado: The
1102 Geological Society of America.
1103 Mallory, W. W. (1958), Pennsylvanian Coarse Arkosic Redbeds and Associated Mountains in
1104 Colorado. In Symposium on Pennsylvanian Rocks of Colorado and Adjacent Areas (pp. 17–
1105 20), Denver, Colorado: Rocky Mountain Association of Geologists.
1106 Maughan, E. K. (1988), Geology and petroleum potnetial, Colorado Park Basin Province, North-
1107 Central Colorado: U.S. Geological Survey Open-File Report 88-450 E.
1108 Mccoy, A., Roy, M., Trevino, L., & Keller, G. R. (2005), Gravity Modeling of the Colorado
1109 Mineral Belt. In K. E. Karlstrom & G. R. Keller (Eds.), The Rocky Mountain Region: An
1110 Evolving Lithosphere Tectonics, Geochemistry, and Geophysics. Washington, D.C.:
1111 American Geophysical Union.

1112 Meqbel, N. M., Egbert, G. D., Wannamaker, P.E., Kelbert, A., & Schultz, A. (2014), Deep
1113 electrical resistivity structure of the northwestern U.S. derived from 3-D inversion of
1114 USArray magnetotelluric data, Earth and Planetary Science Letters, 402, 290-304.
1115 Mitrovica, J. X., Beaumont, C., & Jarvis, G. T. (1989), Tilting of continental interiors by the
1116 dynamical effects of subduction. Tectonics, 8(5), 1079–1094.
1117 Mooney, W. D., & Kaban, M. K. (2010), The North American upper mantle: Density ,
1118 composition , and evolution. Journal of Geophysical Research, 115(B12424), 1–24,
1119 doi:10.1029/2010JB000866.
1120 Nakai, J. S., Sheehan, A. F., & Bilek, S. L. (2017), Seismicity of the rocky mountains and Rio
1121 Grande Rift from the EarthScope Transportable Array and CREST temporary seismic
1122 networks, 2008-2010. Journal of Geophysical Research: Solid Earth, 122, 2173–2192,
1123 doi:10.1002/2016JB013389.
1124 Pakiser, L. C., & Zietz, I. (1965), Transcontinental Crustal and Upper-Mantle Structure. Reivews
1125 of Geophysics, 3(4), 505–520.
1126 Phillips, W. S., Mayeda, K. M., & Malagnini, L. (2014), How to Invert Multi-Band, Regional
1127 Phase Amplitudes for 2-D Attenuation and Source Parameters: Tests Using the USArray.
1128 Pure and Applied Geophysics, 171, 469–484, doi:10.1007/s00024-013-0646-1.
1129 Poe, B. T., Romano, C., Nestola, F., & Smyth, J. R. (2010), Electrical conductivity anisotropy of
1130 dry and hydrous olivine at 8 GPa. Physics of the Earth and Planetary Interiors, 181, 103–
1131 111, doi:10.1016/j.pepi.2010.05.003.
1132 Pommier, A., & Le-Trong, E. (2011), "Sigmelts": A web portal for electrical conductivity
1133 calculations in geosciences. Computers and Geosciences, 37, 1450–1459,
1134 doi:10.1016/j.cageo.2011.01.002.
1135 Porath, H. (1971), Magnetic Variation Anomalies and Seismic Low-Velocity Zone in the
1136 Western United States, Journal of Geophysical Research, 76, 2643-2648.
1137 Porritt, R. W., Allen, R. M., & Pollitz, F. F. (2014), Seismic imaging east of the Rocky
1138 Mountains with USArray. Earth and Planetary Science Letters, 402, 16–25,
1139 doi:10.1016/j.epsl.2013.10.034.
1140 Porter, K. W., & Weimer, R. J. (1982), Diagenetic Sequence Related to Structural History and
1141 Petroleum Accumulation : Spindle Field, Colorado. AAPG Bulletin, 66(12), 2543–2560.
1142 Reitzler, J.S., Gough, D. I., Porath, H., & Anderson III, C. W. (1970), Geomagnetic Deep
1143 Sounding and Upper Mantle Structure in the Western United States, Geophys. J. R. astr.
1144 Soc., 19, 213-235.
1145 Rowe, M. C., Lassiter, J. C., & Goff, K. (2015), Basalt volatile fluctuations during continental
1146 rifting: An example from the Rio Grande Rift, USA. Geochemistry, Geophysics,
1147 Geosystems, 16, 1254–1273, doi:10.1002/2014GC005649.
1148 Rumpfhuber, E., & Keller, G. R. (2009), An integrated analysis of controlled and passive source
1149 seismic data across an Archean-Proterozoic suture zone in the Rocky Mountains. Journal of
1150 Geophysical Research, 114(B08305), 1–25, doi:10.1029/2008JB005886.
1151 Sarafian, E., Evans, R. L., Collins, J. A., Elsenbeck, J., Gaetani, G. A., Gaherty, J. B., Hirth, G.,
1152 & Lizarralde, D. (2015), The electrical structure of the central Pacific upper mantle
1153 constrained by the NoMelt experiment. Geochemistry, Geophysics, Geosystems, 16, 1115-
1154 1132.
1155 Schmandt, B., & Humphreys, E. (2010), Complex subduction and small-scale convection
1156 revealed by body-wave tomography of the western United States upper mantle. Earth and
1157 Planetary Science Letters, 297, 435–445, doi:10.1016/j.epsl.2010.06.047.

1158 Schmandt, B., & Lin, F.-C. (2014), P and S wave tomography of the mantle beneath the United
1159 States. Geophysical Research Letters, 41, 6342–6349, doi:10.1002/2014GL061231.
1160 Schmandt, B., Lin, F.-C., & Karlstrom, K. E. (2015), Distinct crustal isostasy trends east and
1161 west of the Rocky Mountain Front. Geophysical Research Letters, 42,
1162 doi:10.1002/2015GL066593.
1163 Schutt, D., Lowry, A. R., & Buehler, J. S. (2012), The temperature of the western U.S.
1164 lithosphere. In American Geophysical Union Fall Meeting. San Francisco, California:
1165 American Geophysical Union.
1166 Selway, K., Yi, J., & Karato, S.-I. (2014), Water content of the Tanzanian lithosphere from
1167 magnetotelluric data: Implications for cratonic growth and stability. Earth and Planetary
1168 Science Letters, 388, 175-186.
1169 Sheehan, A. F., Abers, G. A., Jones, C. H., & Lerner-Lam, A. L. (1995), Crustal thickness
1170 variations across the Colorado Rocky Mountains from teleseismic receiver functions.
1171 Journal of Geophysical Research, 100(B10), 20391–20404.
1172 Shen, W., Ritzwoller, M. H., & Schulte-Pelkum, V. (2013), A 3-D model of the crust and
1173 uppermost mantle beneath the Central and Western US by joint inversion of receiver
1174 functions and surface wave dispersion. Journal of Geophysical Research: Solid Earth, 118,
1175 1–15, doi:10.1029/2012JB009602.
1176 Shen, W., & Ritzwoller, M. H. (2016), Crustal and uppermost mantle structure beneath the
1177 United States, Journal of Geophysical Research: Solid Earth, 121, 4306-4342,
1178 doi:10.1002/2016JB012887.
1179 Shimojuku, A., Yoshino, T., & Yamazaki, D. (2014), Electrical conductivity of brine-bearing
1180 quartzite at 1 GPa: implications for fluid content and salinity of the crust. Earth, Planets,
1181 and Space, 66(2), 1–9, doi:10.1186/1880-5981-66-2.
1182 Till, C. B., Elkins-Tanton, L. T., & Fischer, K. M. (2010), A mechanism for low-extent melts at
1183 the lithosphere-asthenosphere boundary, Geochemistry Geophysics Geosystems, 11,
1184 doi:10.1029/2010GC003234.
1185 Tweto, O., & Sims, P. K. (1963), Precambrian Ancestry of the Colorado Mineral Belt.
1186 Geological Society of America Bulletin, 74, 991–1014.
1187 van Wijk, J. W., Baldridge, W. S., van Hunen, J., Goes, S., Aster, R., Coblentz, D. D., Grand, S
1188 P., & Ni, J. (2010), Small-scale convection at the edge of the Colorado Plateau:
1189 Implications for topography, magmatism, and evolution of Proterozoic lithosphere.
1190 Geology, 38(7), 611–614, doi:10.1130/G31031.1.
1191 Waff, H. S. (1974), Theoretical Considerations of Electrical Conductivity in a Partially Molten
1192 Mantle and Implications for Geothermometry. Journal of Geophysical Research, 79(26),
1193 4003–4010.
1194 Walker, J. D., Bowers, T. D., Black, R. A., Glazner, A. F., Farmer, G. L., & Carlson, R. W.
1195 (2006), A geochemical database for western North American volcanic and intrusive rocks
1196 (NAVDAT), In A. K. Sinha (Ed.), Geoinformatics: Data to Knowledge: Geological Society
1197 of America Special Paper 397 (pp. 61–71), doi:10.1130/2006.2397(05).
1198 Wannamaker, P. E., Hasterok, D. P., Johnston, J. M., Stodt, J. A., Hall, D. B., Sodergren, T. L.,
1199 Pellerin, L., Maris, V., Doerner, W. M., Groenwold, K. A., & Unsworth, M. J. (2008),
1200 Lithospheric dismemberment and magmatic processes of the Great Basin-Colorado Plateau
1201 transition, Utah, implied from magnetotellurics. Geochemistry, Geophysics, Geosystems,
1202 9(5), doi:10.1029/2007GC001886.

1203 Wannamaker, P. E., Hohmann, G. W., & Ward, S. H. (1984), Magnetotelluric responses of three-
1204 dimensional bodies in layered earths. Geophysics, 49(9), 1517–1533.
1205 Wessel, P. and Smith, W. H. F., (1991), Free software helps map and display data. EOS Trans.
1206 AGU, 72, 441-446.
1207 Wilson, D., Aster, R. C., Ni, J., Grand, S. P., West, M., Gao, W., Baldridge, W. S., & Semken, S.
1208 (2005), Imaging the seismic structure of the crust and upper mantle beneath the Great
1209 Plains, Rio Grande Rift, and Colorado Plateau using receiver functions. Journal of
1210 Geophysical Research, 110(B05306), doi:10.1029/2004JB003492.
1211 Yang, X. (2011), Origin of High Electrical Conductivity in the Lower Continental Crust: A
1212 Review. Surveys in Geophysics, 32, 875–903, doi:10.1007/s10712-011-9145-z.
1213 Yardley, B. W. D., & Valley, J. W. (1997), The petrologic case for a dry lower crust high that
1214 rise to a fluid pressure to the rock that is still hot and ductile , the fluid pressure. Journal of
1215 Geophysical Research, 102(B6), 12173–12185, doi:10.1029/97JB00508.
1216 Yardley, B. W. D., & Valley, J. W. (2000), Reply. Journal of Geophysical Research, 105(B3),
1217 6065–6068.
1218 Yuan, H., French, S., Cupillard, P., & Romanowicz, B. (2014), Lithospheric expression of
1219 geological units in central and eastern North America from full waveform tomography.
1220 Earth and Planetary Science Letters, 402, 176–186, doi:10.1016/j.epsl.2013.11.057.

1221

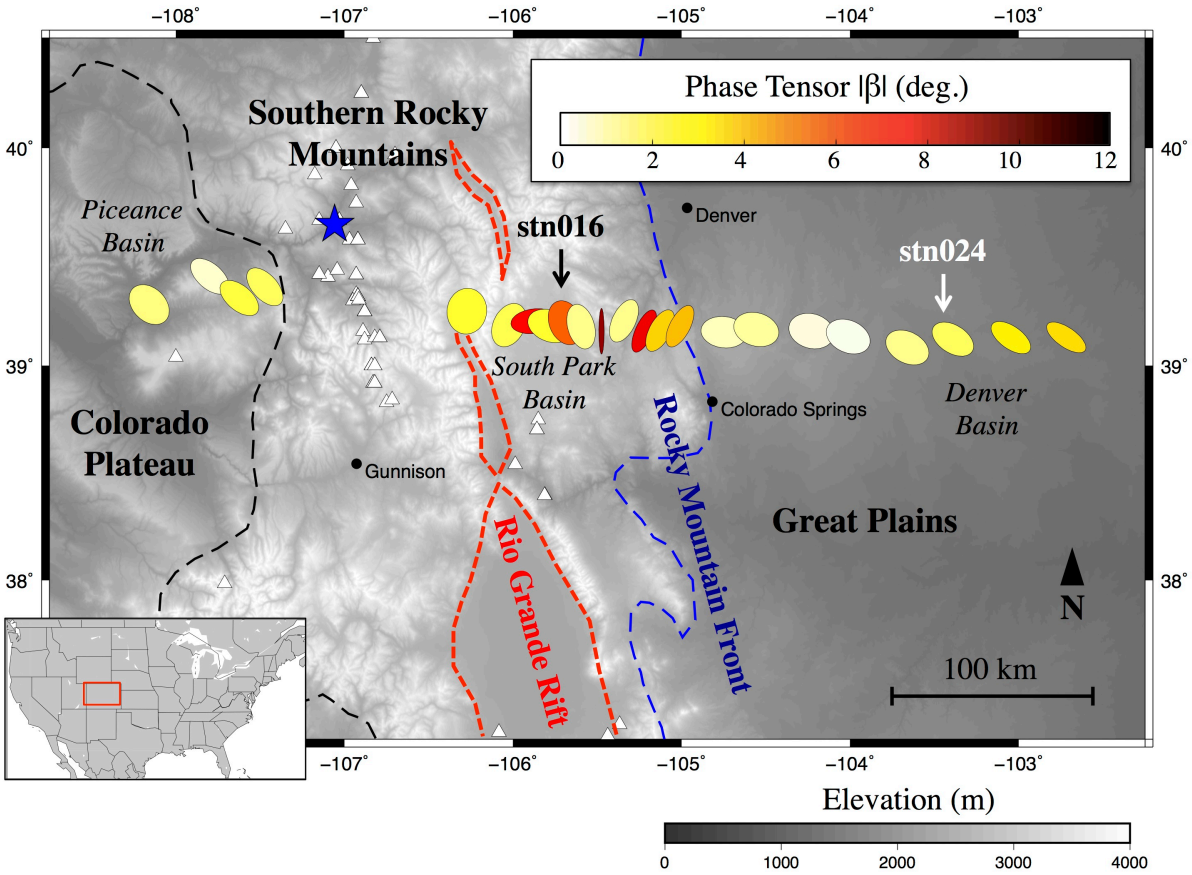

1222

1223 **Figure 1**. Map of magnetotelluric stations in central Colorado. Station locations represented by
1224 normalized magnetotelluric phase tensor ellipses at period of 1000 s. Phase tensor ellipse fill
1225 color is scaled by |β|, with larger values indicating 3D structure. In the presence of 2-D electrical
1226 resistivity structure, the major axis of phase tensor ellipses will align parallel [perpendicular] to
1227 regional geoelectric strike for data collected on the resistive [conductive] side of a geoelectrical
1228 contact. Note the 90º rotation of the phase tensor ellipses across the Rocky Mountain Front [blue
1229 dashed line] that separates resistive basement-cored uplifts to the east from conductive
1230 sedimentary units of the Denver Basin to the west. Red dashed lines are approximate outlines of
1231 axial basins of the Rio Grande Rift. Black and blue dashed lines are physiographic province
1232 boundaries [*Fenneman*, 1946]. Blue star is location of Quaternary basalt flow near Dotsero, CO
1233 [see Section 4.2]. White triangles are young volcanics [<10 Ma] from the NAVDAT database
1234 [*Walker et al*., 2006]. Location of MT data shown in Figure 2 indicated by arrows and station
1235 labels.

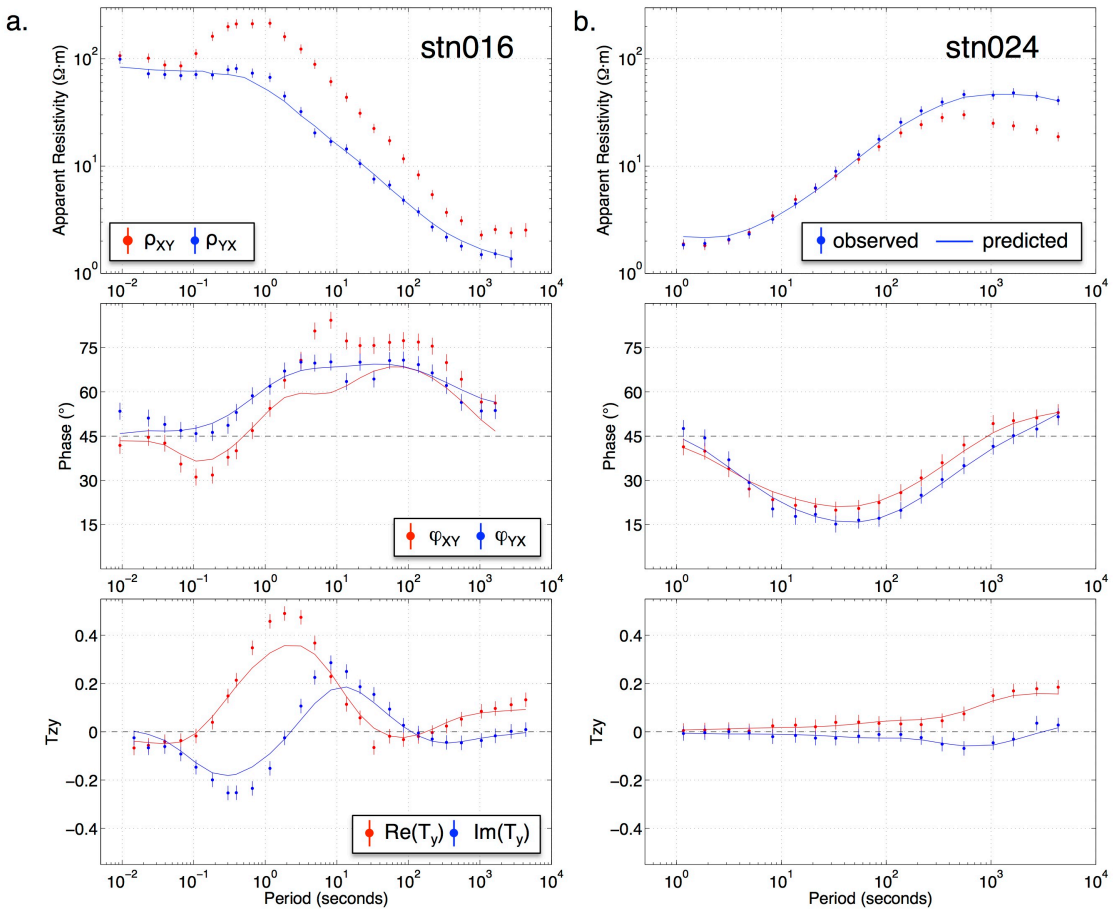

Figure 2. MT apparent resistivity, phase, and tipper [T_Y] [data points with 1 sigma uncertainty] and 2D anisotropic model fits [solid lines] for stations [a] 016 in the mountains and [b] 024 in the plains. TE mode apparent resistivity [ρ_{XY}] omitted from the inversion inputs to reduce influence of 3D electrical resistivity structure.

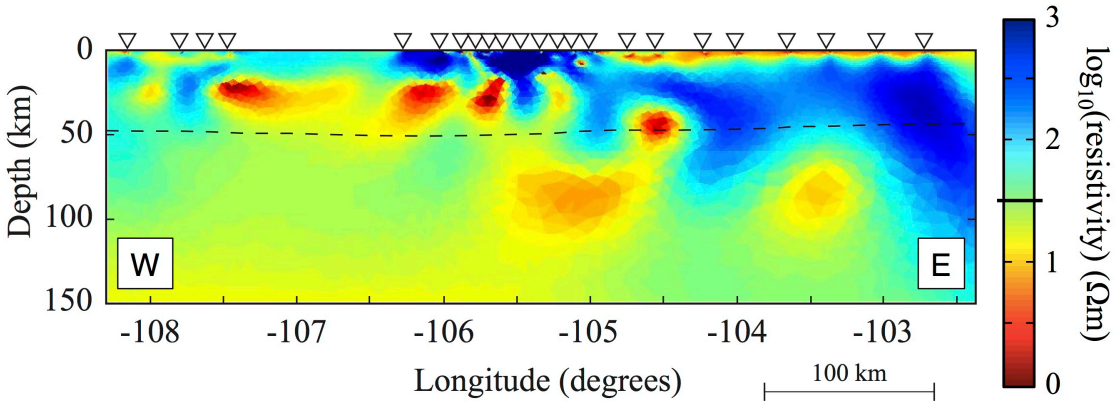

Figure 3. 2D isotropic electrical resistivity model. Black dashed line is Moho estimate from *Shen et al*. [2013]. Note alternating pattern of vertical resistors and conductors suggestive of anisotropic resistivity structure in the lower crust [Supplementary Material, Figure S2]. Inverted white triangles indicate MT station locations. Bold line on resistivity color bar indicates starting model resistivity of 30 Ωm.

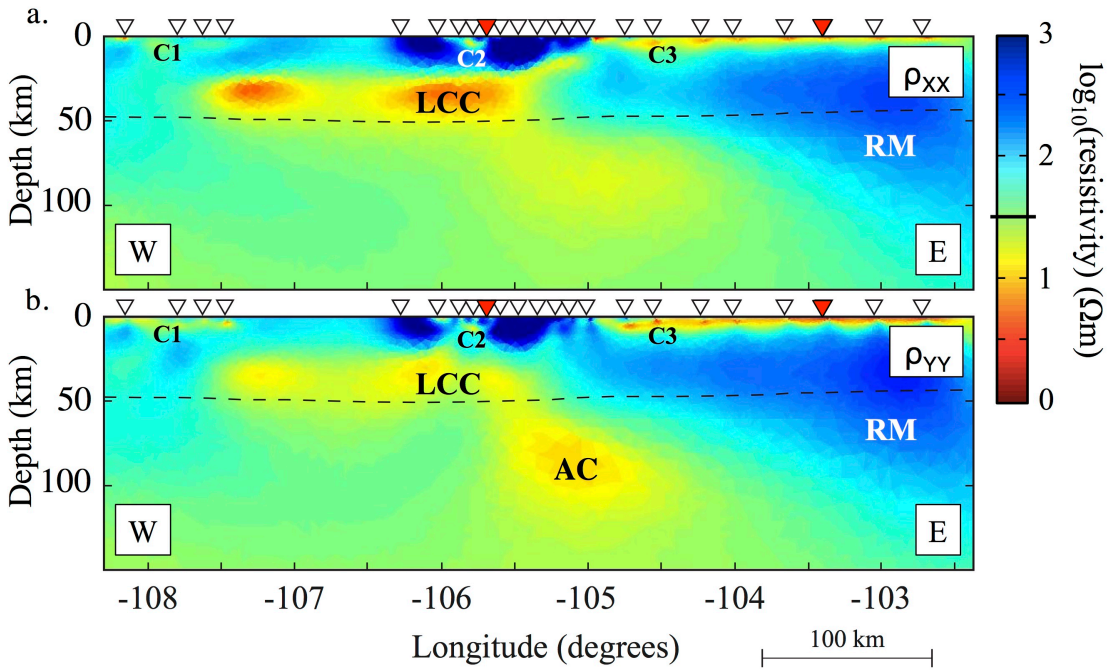

Figure 4. 2D anisotropic electrical resistivity models. Models for resistivity in [a] N-S [ρ_{xx}] and [b] E-W [ρ_{yy}] directions. Annotations as in Figure 3 plus red triangles denote along-profile location of stations shown in Figure 2. LCC = lower crustal conductor, RM = resistive mantle, AC, C1, C2, C3 = low resistivity anomalies [see text].

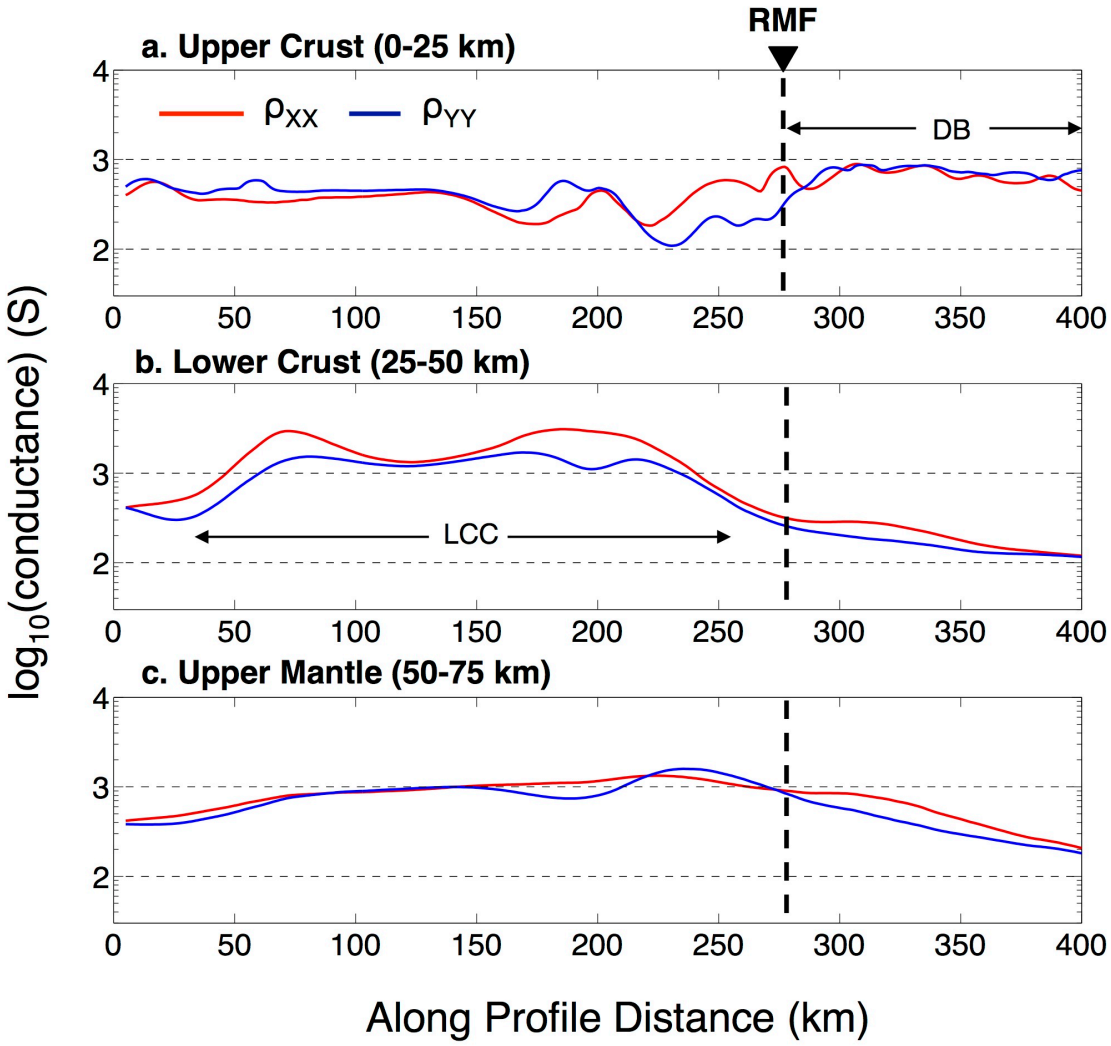

Figure 5. Vertically-integrated conductance [conductivity-thickness product] of final [ρ_{xx}] and [ρ_{yy}] resistivity models in Figure 4 for [a] upper crust [0-25 km depth], [b] lower crust [25-50 km depth], and [c] upper mantle [50-75 km depth]. Bold dashed line indicates location of Rocky Mountain Front [RMF]. Conductance along profile shown as separate lines for ρ_{xx} and ρ_{yy} resistivity models, with separation between lines indicating degree of anisotropy. Along profile distance = 0 corresponds to location of westernmost station at approximately (39.2ºN, 108.2ºW). DB = Denver Basin, LCC = lower crustal conductor.

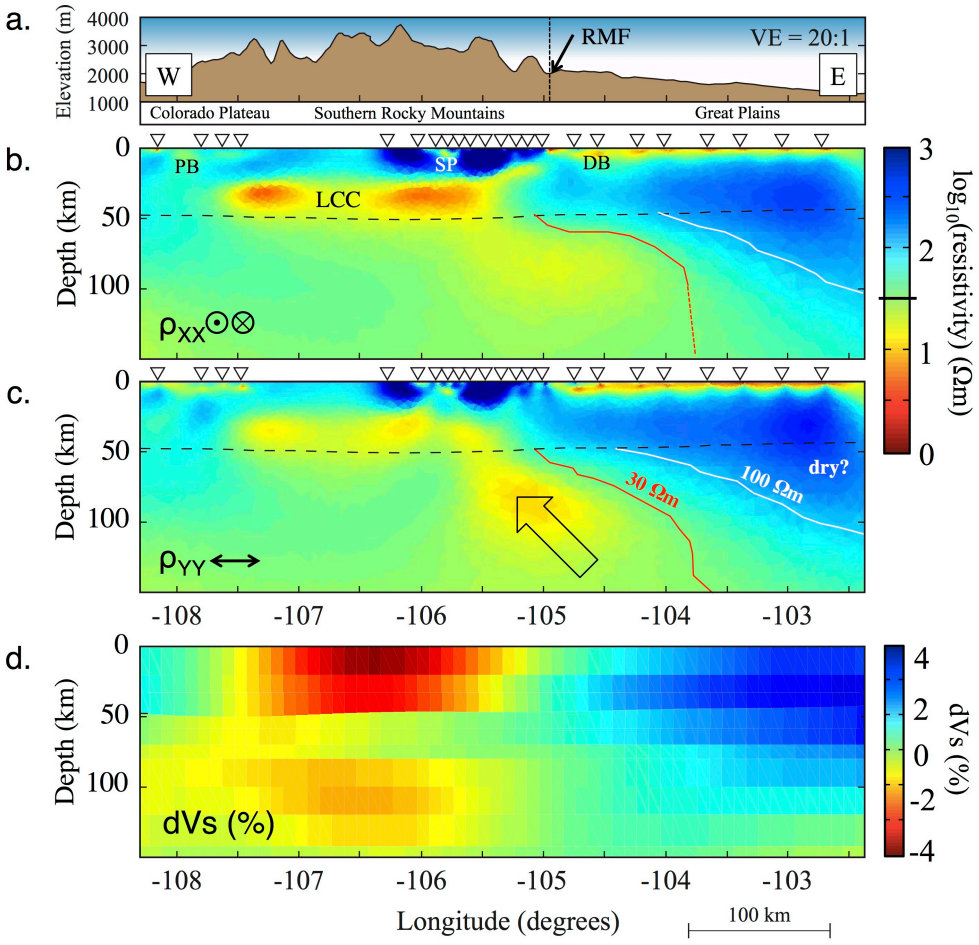

Figure 6. Interpretation of anisotropic electrical resistivity model and comparison to seismic tomography. Resistivity models are identical to Figure 4 for [b] N-S [ρ_{xx}] and [c] E-W [ρ_{yy}] directions. Shear wave velocity perturbation relative to a 1D-starting model from *Li et al.*, [2002] shown in [d]. Topography and approximate physiographic province boundaries along profile are indicated in [a]. Annotations as in Figure 3 plus white and red lines are approximate resistivity contours for 30 and 100 Ωm, respectively, in the mantle. Arrow in ρ_{yy} model indicates supply of heat, melt, and/or volatiles to the lithospheric mantle. LCC = lower crustal conductor; DB = Denver Basin; SP = South Park Basin; PB = Piceance Basin; RMF = Rocky Mountain Front.

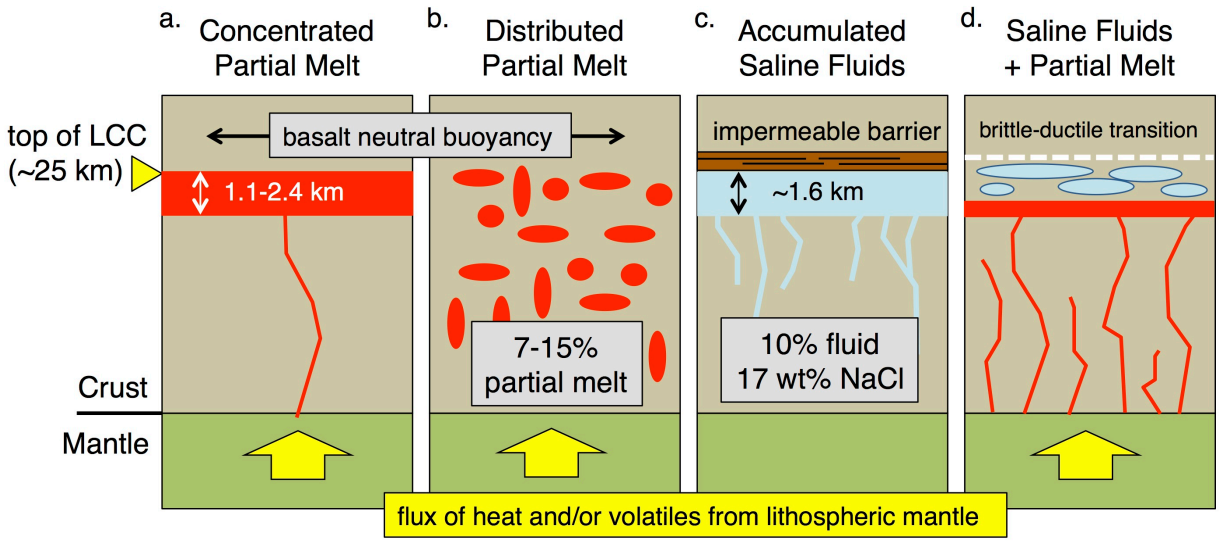

Figure 7. Collection of partial melt and/or fluid distributions that could produce the high conductivity observed in the lower crust beneath the Rocky Mountains. Including: a series of molten sills [a], distributed partial melt [b], saline fluid ponding beneath an impermeable barrier to upward fluid flow [c], and intermediate combinations of ponded fluid and distributed and/or ponded partial melt. Yellow arrow represents supply of heat and/or volatiles driving production of melt in lithospheric mantle. Preferred interpretation most closely resembles [d] [see text for details].

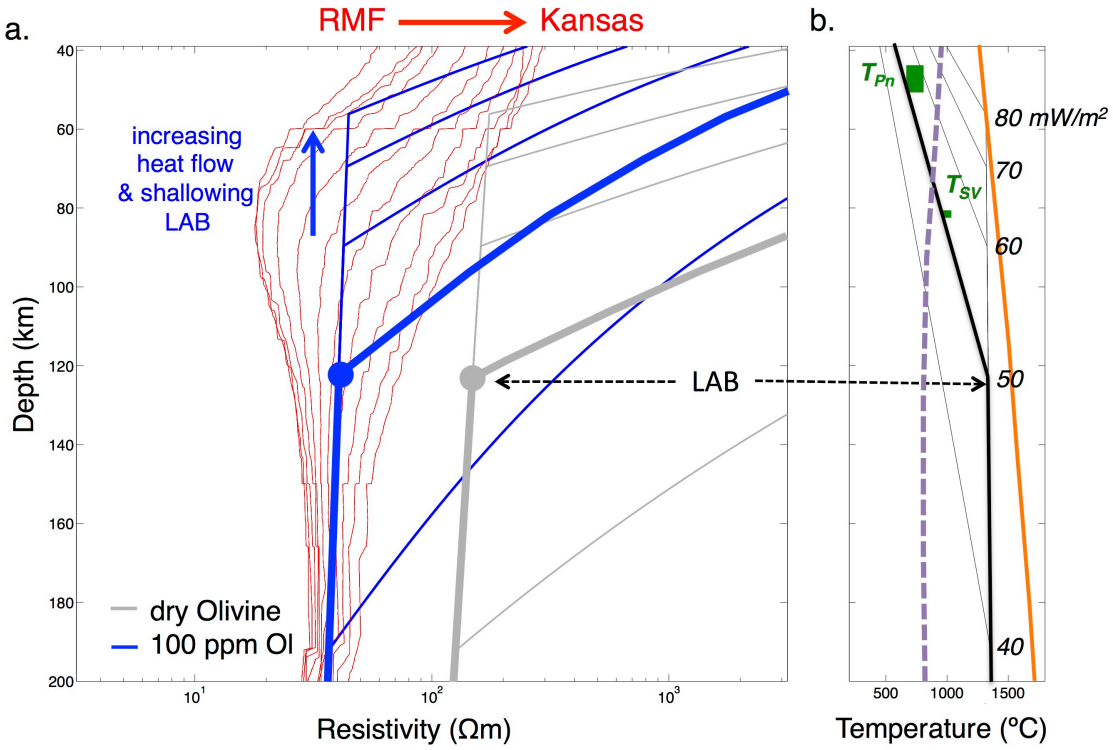

Figure 8. Mantle resistivity vs. lithospheric hydration. Red lines in [a] are resistivity-depth profiles extracted from Great Plains region of ρ_{xx} model in Figure 4a. Red arrow indicates increasing upper-mantle resistivity with eastward progression of profiles from the Rocky Mountain Front [RMF] to near the Colorado-Kansas border. Blue and gray lines are electrical resistivity models [*Gardes et al*., 2014] for dry [gray] and hydrated [100 ppm H_2O] mantle olivine subject to range of assumed continental geotherms in [b] [*Hasterok and Chapman*, 2011]. Multiple lines in [a] and [b] show the effect of geothermal gradient on resistivity profiles. Geotherms are defined by surface heat flow values [indicated in (b) in units of mW/m^2 at depth that mantle lithosphere geotherm intersects mantle adiabat].. Bolded lines in [a] represent resistivity model corresponding to preferred geotherm bolded in [b] [50 mW/m^2]. Preferred geotherm justified by surface heat flow and independent seismically-derived estimates of mantle temperature [green squares] from *Hansen et al.* [2015] [T_{SV}] and *Schutt et al.* [2012] [T_{Pn}]. Dashed horizontal line is estimated depth of lithosphere-asthenosphere boundary [LAB] determined from change in slope of geotherm [i.e. depth of transition from conductive to convective geotherm]. Orange line is peridotite dry solidus [*Hirschmann* 2000] and purple line is peridotite saturated solidus [*Till et al*., 2010]

Journal of Geophysical Research: Solid Earth

Supporting Information for

Magnetotelluric imaging of lower crustal melt and lithospheric hydration in the Rocky Mountain Front transition zone, Colorado, USA

D. W. Feucht[1,2], A. F. Sheehan[1,2], and P. A. Bedrosian[3]

[1]Department of Geological Sciences, University of Colorado Boulder, Boulder, Colorado, USA, [2]Cooperative Institute for Research in Environmental Sciences, University of Colorado Boulder, Boulder, Colorado, USA, [3]Crustal Geophysics and Geochemistry Science Center, U.S. Geological Survey, Denver, Colorado, USA.

Contents of this file

Introduction

Supporting information includes magnetotelluric data acquisition parameters, additional data visualization including tippers (Fig. S1) and pseudo-sections of data and model response (Fig. S5), and model sensitivity tests performed to justify interpretation of anisotropic electrical resistivity models. Also included are two figures in support of the interpretation: a plot of bulk resistivity vs. melt fraction for basaltic melt of varying water content (Fig. S6) and a comparison of three regional scale seismic velocity model cross sections co-located with the MT profile (Fig. S7).

S1. Data Acquisition and Survey Parameters

Time series data at each MT site were recorded for two orthogonal components of the horizontal electric field and three orthogonal components of the magnetic field at each station location. Broadband magnetotelluric data (100 Hz - 1000 s) were collected using Electromagnetic Instruments low-frequency MT24 data loggers and three orthogonal Schlumberger magnetic induction coils. Long period MT data (10 - 11,000 s) were collected using NIMS data loggers and three-component fluxgate magnetometers. Electric field measurements were collected using two orthogonal 100 m dipoles each consisting of two non-polarizing electrodes connected by copper wire. Broadband instruments were allowed to record for 24-48 hours while long period instruments recorded for three to six weeks. Of the 23 stations, six were instrumented with only broadband equipment, seven with only long-period equipment, and ten with both. Nominal station spacing was 5-10 km near the center of the profile and more distributed (up to 30 km spacing) on the eastern and western ends of the profile. Data were collected simultaneously at several (2-4) stations to permit multi-station remote-reference processing [*Egbert*, 1997; *Gamble et al*., 1979].

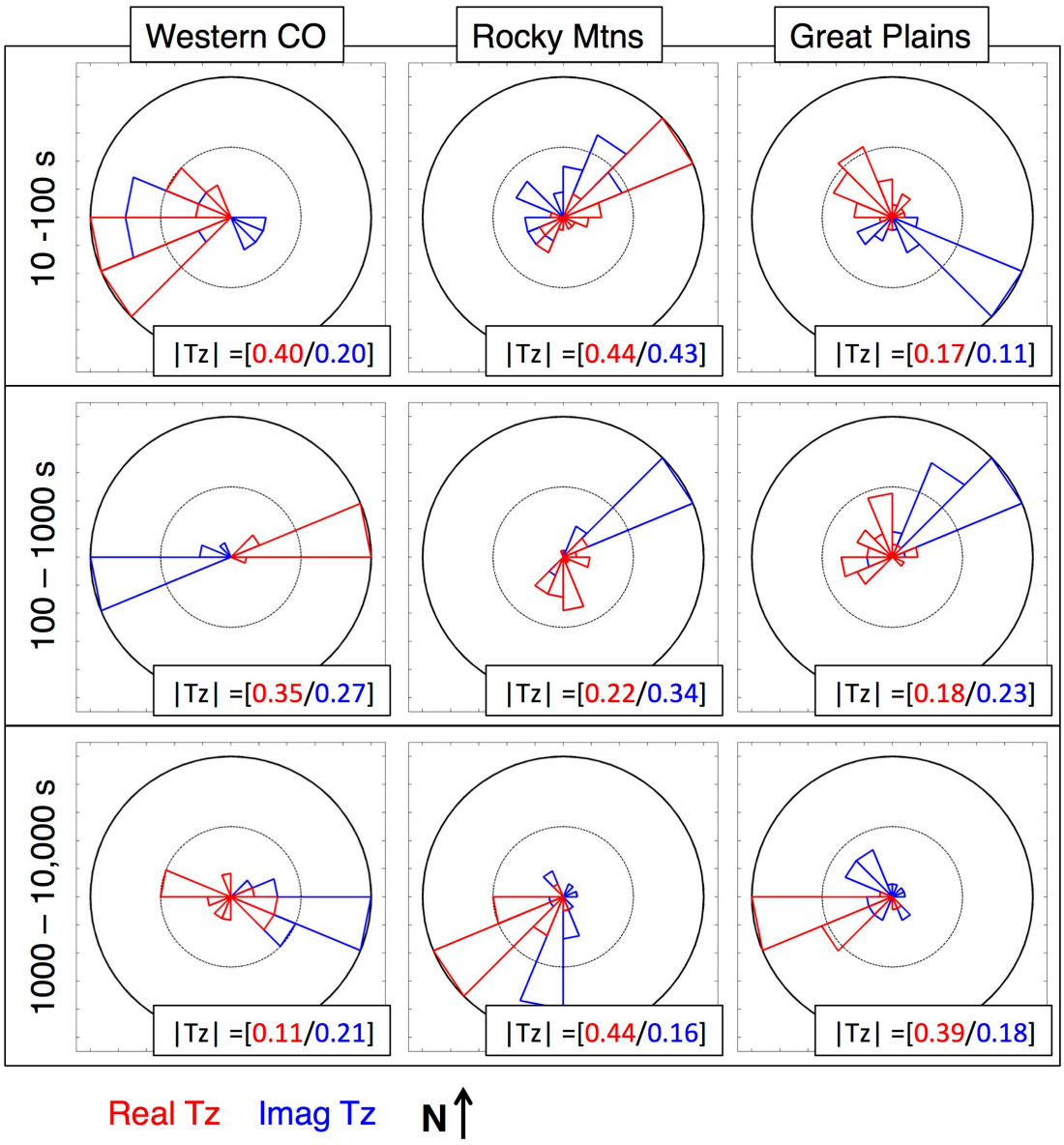

Figure S1. Induction vector rose diagrams. Data are grouped by longitude [columns] and period range [rows]. Each diagram shows a rose histogram of induction vector azimuth for both real [red] and imaginary [blue] components. Induction vectors are displayed in the Parkinson-convention [i.e. pointing towards conductors] and bin counts are normalized to maximum bin count for each individual plot. Longitudinal groupings are Western Colorado (CO) [all stations west of -107°W; n = 4], Great Plains [all stations east of -105°W; n = 8], and Rocky Mountains [all stations between -107 and -105°W; n = 11]. Average tipper magnitudes (|Tz|) are provided for the real and imaginary induction vectors within each plot. Tippers with magnitude > 1.0 were excluded to account for noise. The lower crustal conductor in Figures 4 and 6 is located beneath the Rocky Mountain stations and the two easternmost Western Colorado stations. Assumed regional geo-electric strike is north-south.

S2. Model Sensitivity to the Lower Crustal Conductor

Forward modeling tests were performed to investigate three aspects of the lower crustal conductor as it appears in our preferred model: (1) the sensitivity of the data to total conductance of the LCC, rather than absolute conductivity or thickness, (2) the lateral continuity of the conductor across the station gap from approximately 106.25ºW to 107.5ºW and (3) the necessity of anisotropic modeling. A series of simple forward models were created with features approximating the main resistivity structure of the preferred ρ_{xx} model in Figure 4a. These features included a conductive Denver Basin, a resistive crust, a lower crustal conductor, and a resistive mantle keel beneath the plains. The thickness, electrical resistivity, lateral connectivity, and anisotropy of the LCC were varied for each forward model while the remaining features were held fixed. Sensitivity testing was carried out as follows: (1) synthetic MT responses were generated for each forward model at along-profile distances and periods corresponding to those available in the real data set, (2) random noise and error bars were added to the synthetic responses, and (3) the synthetic data were inverted for isotropic resistivity structure using the same mesh, starting model, and inversion parameters as described in Section 2. The first synthetic test included modeling the synthetic data using the anisotropic inversion parameters described in Section 2. For simplicity, anisotropy was not included in the second and third synthetic tests (i.e. the anisotropy penalty factor was fixed at 1.0).

Figure S2 shows the results of the test performed to assess the need for anisotropic modeling. Figure S2a shows the anisotropic forward model used for this synthetic test. Note that only the lower crustal conductor is anisotropic and that the degree of anisotropy is relatively modest (0.5 decades in $\log_{10}$(resistivity)). Figure S2b shows that MARE2DEM successfully reproduces the anisotropic resistivity structure of the lower crust from an initially isotropic half-space starting model using an anisotropy factor of 0.1. Figure S2c shows that isotropic modeling of anisotropic data introduces artifacts into the resistivity structure of the anisotropic regions of the model, namely a vertical stripping pattern of alternating resistive and conductive bodies. The similarities between Figure S2c and the isotropic inversion result in Figure 3 motivated the use of anisotropic inversion in this study.

The results of the test on sensitivity to conductance are shown in Figure S3. Each of the five forward models used for this test was parameterized with a laterally continuous conductor, the top of which was fixed at a depth of 25 km. The thickness of the conductor was varied from 300 m to 30 km while the resistivity was varied from 0.15 Ωm to 15 Ωm to maintain a total conductance of ~2000 S (the contribution of any remaining resistive lower crust to the total conductance was minimal, reaching a maximum of 100 S for the model with the thinnest conductor). Four out of the five models produced from inverting the various synthetic MT data sets are nearly identical (Figure S3b-e) despite vast differences in the geometry and electrical properties of the LCC. The most distinct result (Figure S3e) was obtained for the only synthetic model with the LCC in contact with the conductive upper mantle. Figure S3g shows the integrated lower crustal conductance for each of the five forward models alongside that of the preferred ρ_{xx} model from the anisotropic inversion of the measured data. From this we conclude that our data are primarily sensitive to the total conductance of the LCC rather than its absolute resistivity or thickness.

The results of the test on lateral continuity of the conductor are shown in Figure S4. Each of the five forward models used for this test was parameterized with a 10 km thick lower crustal conductor with resistivity of 5 Ωm. A lateral resistive "tear" was inserted into each conductor, with the width of the tear varying for each forward model from 15-75 km. The tear was centered at the midpoint between the two stations bounding the ~100 km gap in station coverage (Figure 1). As shown in Figure S4b-f, the resistive tear was successfully imaged in each synthetic test. The inversion result from Figure S3e is reproduced in Figure S4g to show the case of a laterally continuous conductor of the same thickness and resistivity. Figure S4h shows the total lower crustal conductance for the models in Figure S4b-g and the ρ_{xx} model in Figure 4. From this we

conclude that the apparent gap in the lower crustal conductor within the anisotropic inverse model is a reflection of the station coverage and is to be expected even for a laterally continuous conductor. That the model with a laterally continuous conductor does the best job of reproducing the lower crustal conductance curve of the ρ_{xx} model suggests that the lower crustal conductor is laterally continuous.

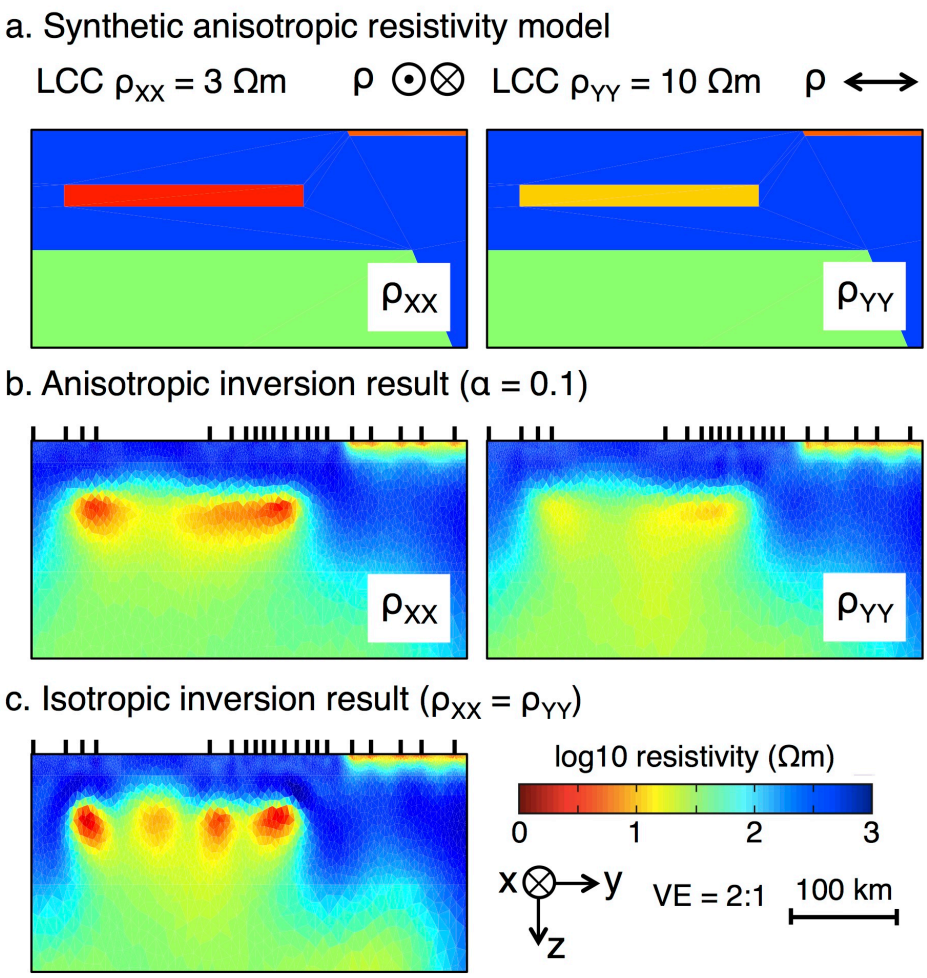

Figure S2. Results of the test for MARE2DEM response to anisotropic resistivity structure. An anisotropic forward model [a] representing a simplified version of the preferred ρ_{xx} model in Fig. 4, in this case with a 10 km thick lower crustal conductor with resistivity 3 Ωm in the x-direction [N-S] and 10 Ωm in the y-direction [E-W]. Results of inverting synthetic anisotropic data using anisotropic [b] and isotropic [c] inversion parameters. Note similarity between lower crustal structure in [c] to isotropic inversion results in Fig. 3. Approximate model view is surface to 100 km depth and 0 to 400 km along profile. Tick marks on [b] and [c] indicate location of synthetic MT data corresponding to relative location of MT stations in the real data set.

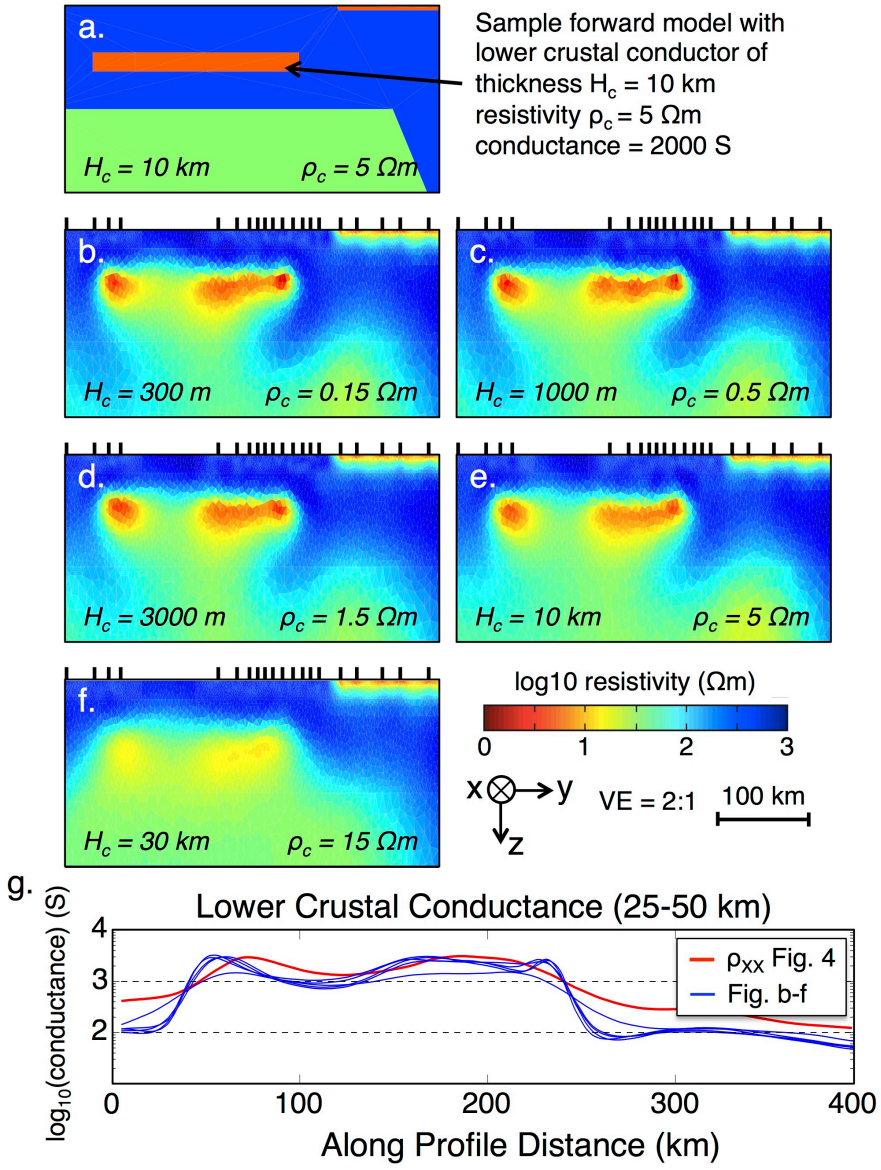

Figure S3. Results of the test for sensitivity to lower crustal conductor [LCC] thickness and resistivity. A sample isotropic forward model [a] representing a simplified version of the preferred ρ_{xx} model in Figure 4a, in this case with a 10 km thick lower crustal conductor with resistivity 5 Ωm. Each of [b]-[f] represents the result of inverting synthetic forward models with different LCC thicknesses [Hc] and resistivity values [ρc] as labeled on each model. Vertically integrated lower crustal conductance is shown in [g] for the ρ_{xx} model in Fig. 4a [25-50 km depth] and each of the synthetic inversion results in Figure S3[b]-[f] [25-55 km depth]. Approximate model view is identical to Figure S2. Tick marks on [b]-[f] represent MT station locations as in Figure S2.

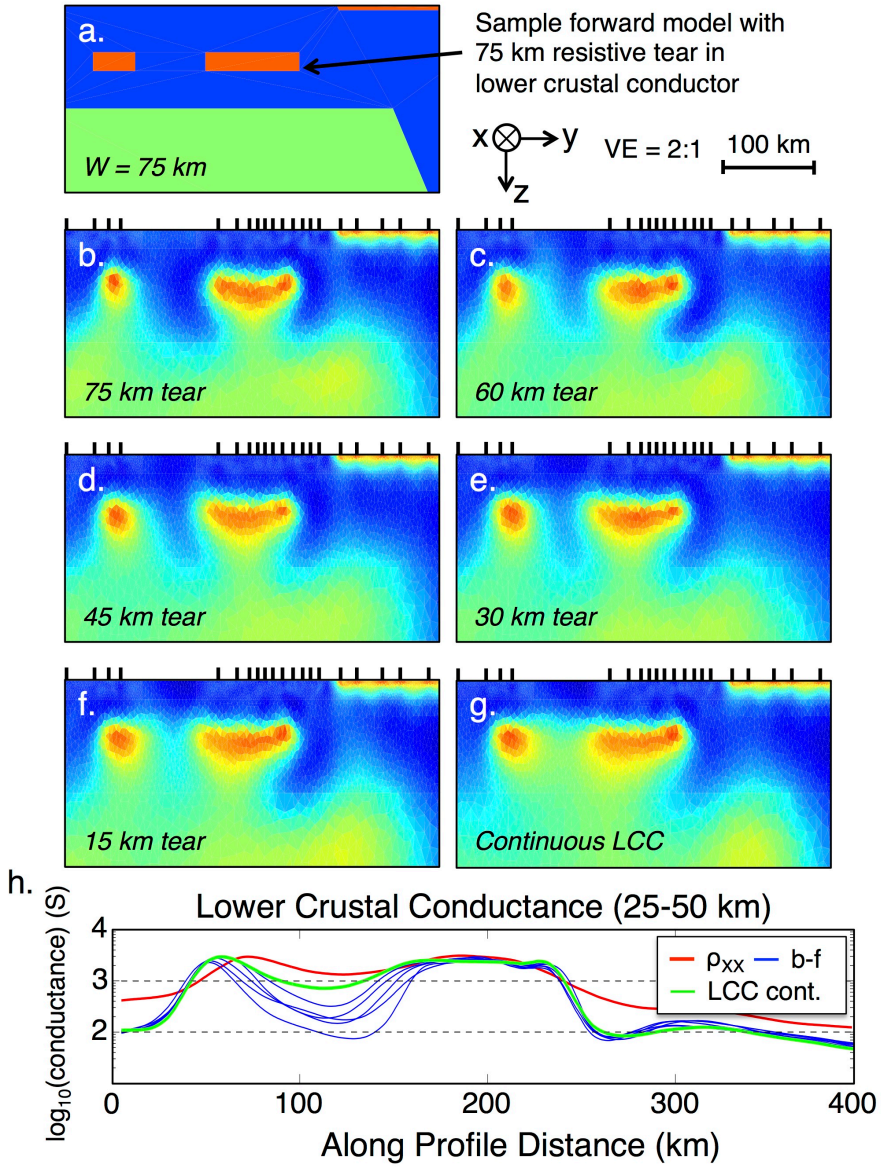

Figure S4. Results of the test for sensitivity to lateral continuity of the lower crustal conductor. A sample isotropic forward model [a] representing a simplified version of the preferred ρ_{xx} model in Figure 4a, in this case with a 75 km wide resistive tear centered on the location approximating the western Colorado station gap evident in Figure 1. Each of [b]-[f] represents the result of inverting synthetic forward models with different tear widths as labeled on each model. Conductor thickness and resistivity is fixed for these models. The synthetic results from Figure S3[d] are provided in [g] for comparison to the case of a laterally continuous conductor of similar thickness and resistivity. Vertically integrated lower crustal conductance is shown in [h] for the ρ_{xx} model in Fig. 4a [25-50 km depth] and each of the synthetic inversion results in Figure S4[b]-[f] [25-55 km depth]. Resistivity color scale and approximate model view are identical to Figure S2. Tick marks on [b]-[g] represent MT station locations as in Figure S2.

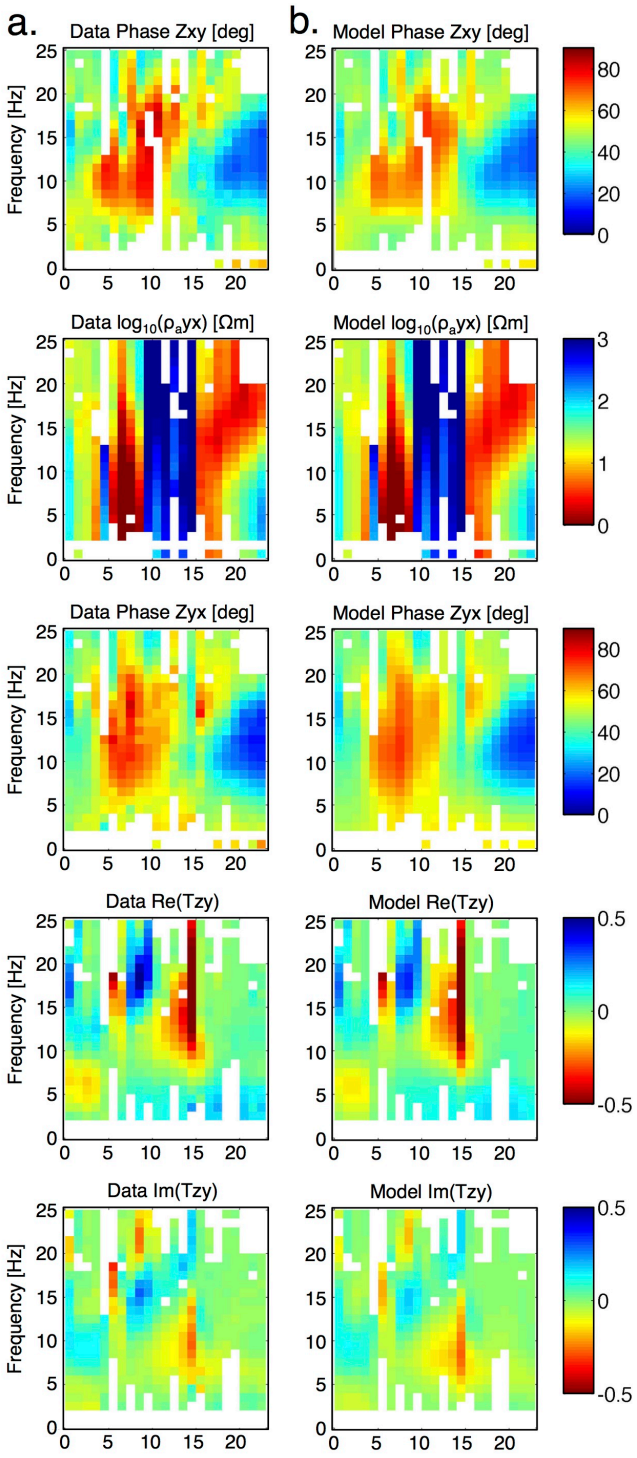

Figure S5. Pseudo section plots of data [a] and forward model response [b] of preferred anisotropic model. Magnetotelluric transfer functions are plotted at all stations as a function of period [high frequency at top] and along profile station order from west [0] to east [23]. Note that tipper is unit less.

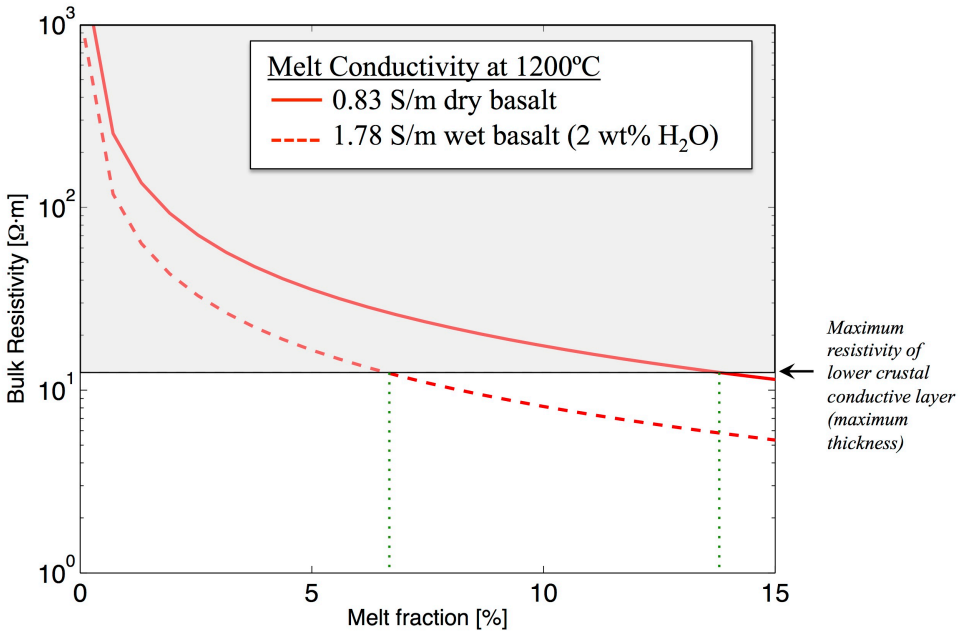

Figure S6. Trade-off between bulk resistivity of imaged MT anomaly and melt fraction of dry and wet basalt at 1200ºC. Based on equations from *Waff* [1974] assuming 100% interconnected melt, small melt fraction, and resistive mineral grains. Melt conductivity calculated using SIGMELTS [*Pommier and Le-Trong*, 2011]. Melt conductivity parameters derived from petrologic and geophysical data [see references in text]. Dashed line represents maximum electrical resistivity of our lower crustal conductor, which corresponds to the end-member case of melt distributed uniformly from the Moho to 25 km depth. Green dashed lines indicate minimum melt fractions for basaltic melt that is either wet [~7%] or dry [~14%]. Vertically confined melt layers [i.e. layers less than ~25 km thick] would require higher melt fractions if partial melt is the only contributor to low resistivity in the lower crust.

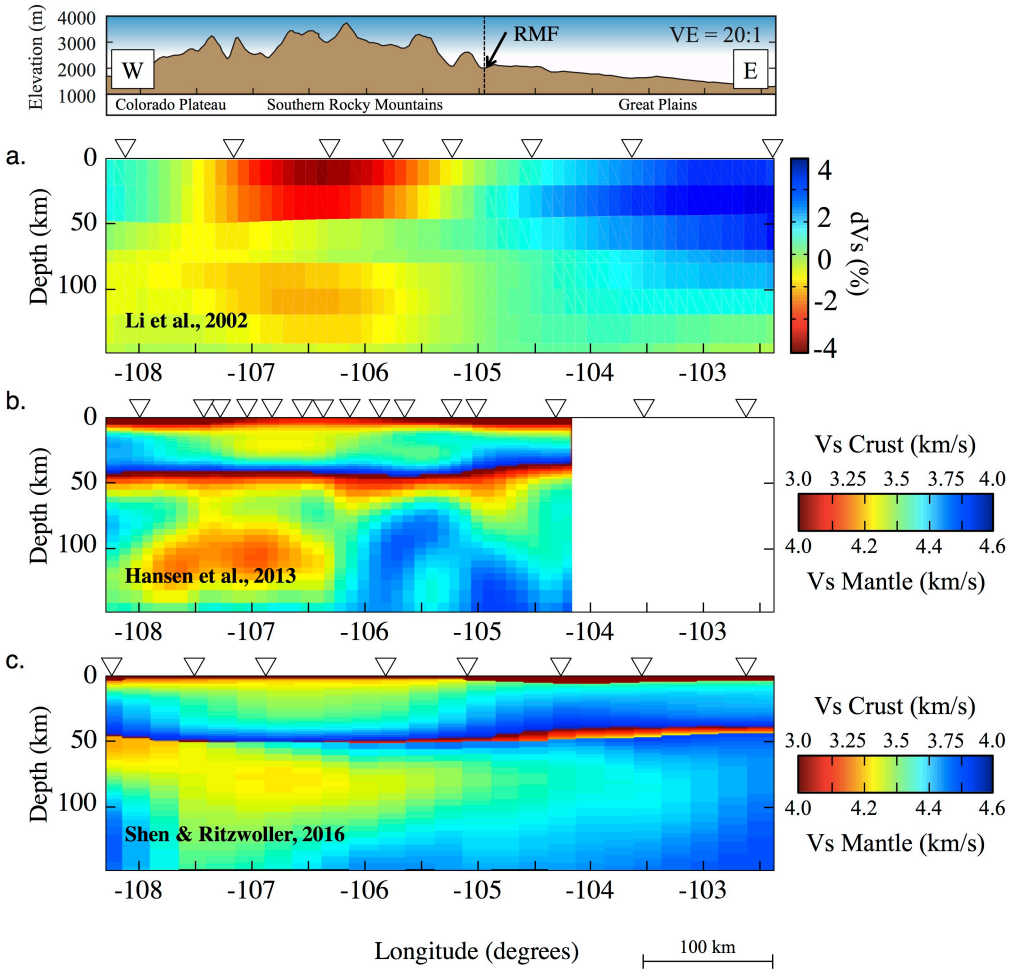

Figure S7. Comparison of regional scale seismic tomography studies in the area of interest from [a] *Li et al*. [2002], [b] *Hansen et al*. [2013], and [c] *Shen and Ritzwoller* [2016]. Color scale in [a] is shear velocity perturbation relative to a 1D-starting model modified from AK135. Color scale in [b] and [c] is absolute shear velocity [3-4 km/s in the crust; 4-4.65 km/s in the mantle]. Starting models for *Hansen et al*. [2013] and *Shen and Ritzwoller* [2016] are simple 4.4 km/s half space. White triangles represent approximate seismometer locations along or adjacent to profile for each experiment [note denser station spacing in (b)]. Model view is identical to that shown for the anisotropic MT model in Figure 6. Along profile topography and approximate physiographic province boundaries are indicated, including the location of the Rocky Mountain Front (RMF) at approximately -105ºW.